

High speed infrared thermography to investigate heat transfer of transonic turbine rotor blades

Sisti, Manuela; Falsetti, Chiara; Beard, Paul F.

DOI

[10.1016/j.measurement.2025.118103](https://doi.org/10.1016/j.measurement.2025.118103)

Publication date

2025

Document Version

Final published version

Published in

Measurement: Journal of the International Measurement Confederation

Citation (APA)

Sisti, M., Falsetti, C., & Beard, P. F. (2025). High speed infrared thermography to investigate heat transfer of transonic turbine rotor blades. *Measurement: Journal of the International Measurement Confederation*, 256, Article 118103. <https://doi.org/10.1016/j.measurement.2025.118103>

Important note

To cite this publication, please use the final published version (if applicable). Please check the document version above.

Copyright

Other than for strictly personal use, it is not permitted to download, forward or distribute the text or part of it, without the consent of the author(s) and/or copyright holder(s), unless the work is under an open content license such as Creative Commons.

Takedown policy

Please contact us and provide details if you believe this document breaches copyrights. We will remove access to the work immediately and investigate your claim.



High speed infrared thermography to investigate heat transfer of transonic turbine rotor blades

Manuela Sisti^{a,c} , Chiara Falsetti^b , Paul F. Beard^{a,*} 

^a University of Oxford, Department of Engineering Science, Oxford Thermofluids Institute, OX2 0ES Oxford, United Kingdom

^b Delft University of Technology, Department of Aerospace Engineering, Propulsion and Power, Postbus 5, 2600 AA Delft, Netherlands

^c University of Tokyo, Department of Aeronautics and Astronautics, 7-3-1 Hongo, Bunkyo-ku, Tokyo, 113-8656, Japan

ARTICLE INFO

Keywords:

Infrared thermography
Gas turbine
Rotor
Heat transfer
OTRF
High-speed
Turbomachinery
Measurement advancements

ABSTRACT

The role of infrared (IR) thermography has become increasingly predominant in aerothermal testing of gas turbine components in non-rotating engine representative experiments. However, efforts are ongoing to achieve accurate measurements in rotating experiments with target speeds in excess of ~ 200 m/s and surfaces temperatures below 500 K. A novel measurement system employing IR thermography was developed for the Oxford Turbine Research Facility (OTRF), a UK national engine-representative high-pressure turbine test facility operating with rotational speed of 8,500 rpm and transonic flow. The infrared measurements focussed on estimating the temperatures of uncooled blade squealer tips with a target velocity of 263.5 ms^{-1} . The aerothermal design of this region is key for engine efficiency and blade life. Correction of all sources of errors are applied to the IR raw thermal data, obtaining results as two-dimensional maps of target temperature following procedures developed by Sisti et al. [1]. A range of camera integration times varying from 20 to $1 \mu\text{s}$ was tested to investigate the effect on image quality and measurement accuracy, allowing deeper understanding on the effects of noise, detector undersaturation and image blur. Results obtained with an integration time of 20, 10, 5, 2, and $1 \mu\text{s}$ are firstly compared as blackbody equivalent temperatures. Subsequently, data acquired with camera integration time of 10, 5, and $1 \mu\text{s}$ is processed to scalable heat transfer quantities (i.e. adiabatic wall temperature and Nusselt number) for the first time in literature for a turbine blade in rotating, transonic test facility. Finally, a detailed post-test uncertainty analysis is presented. This study demonstrates the capability of IR to capture temperature and heat transfer phenomena at high speed in gas turbine research and highlights the impact of the camera integration time on image quality and temperature measurement accuracy.

1. Introduction

There is significant potential for improving gas turbine aerothermal performance, possibly leading to a 30% increase in overall efficiency compared to current best-in-service engines [2], with consequential reduction of CO₂ emissions, whilst the adoption of Sustainable Aviation Fuels (SAF) or Hydrogen as aviation fuels is more commercially viable. Achieving this level of progress requires advancement in various fields. In terms of thermodynamic efficiency this primarily translates into increased Turbine Entry Temperature (TET), which revolves around achieving efficient combustion, more advanced thermal management solutions, and improved material capabilities. The main strategy employed to overcome the limitation on increasing TET due to component failure is the implementation of cooling technologies. The

development of such cooling schemes is often researched and proven in engine representative experiments, such as those conducted at the Oxford Turbine Research Facility (OTRF), providing aerothermal testing of rotating axial gas turbines.

Over the years, several techniques for measuring temperature have been conceived with the purpose of achieving accurate readings of thermal interactions. Widely used methods include thermocouples, thin-film gauges, thermochromic liquid crystals, temperature and pressure sensitive paints, thermal paints, and infrared thermography. While thermocouples and thin-film gauges are extensively used to perform single-point measurements on stationary components, they both present a list of challenges when used on rotating or fast-moving components. Both measurement techniques require wiring access, and thin film gauges require time consuming soldering and complicated calibration, signal conditioning electronics and data processing. Sensor integrity is

* Corresponding author.

E-mail addresses: manuelasisti@g.ecc.u-tokyo.ac.jp (M. Sisti), c.falsetti@tudelft.nl (C. Falsetti), paul.bead@eng.ox.ac.uk (P.F. Beard).

Nomenclature*Abbreviations*

FPA	Focal Plane Array
FOV	Field of View
HP	High Pressure
IR	Infrared
IT	Integration Time
LWIR	Long-Wave Infrared
OTRF	Oxford Turbine Research Facility
PEEK	PolyEtherEtherKetone
px	Pixel
PS	Pressure Side
ROI	Region of Interest
TET	Turbine Inlet Temperature

Roman Symbols

c_{true}	True chord, m
d^*	Nondimensional blur
h	Convective heat transfer coefficient, $W m^{-1} K^{-1}$
k_{air}	Thermal conductivity of air, $W m^{-1} K^{-1}$
N	Speed, rpm
Nu	Nusselt Number

p	Pressure
\dot{q}	Heat flux, $W m^{-2}$
t	Time, s
T	Temperature, K
v_t	Tangential velocity, $m s^{-1}$
U	Uncertainty value

Greek Symbols

ε	Surface emissivity
τ	Transmissivity
σ	Stefan-Boltzmann constant

Subscripts

0	Total conditions
1	Value related to surface 1
2	Value related to surface 2
<i>aw</i>	Adiabatic wall value
<i>bb</i>	Blackbody value
<i>cam</i>	Equivalent blackbody value recorded by camera
<i>opt</i>	Optical path value
<i>r</i>	Reflected value
<i>t</i>	Target value

also often an issue, for example under the high centrifugal forces on the rotor blade. The introduction of optical measurement techniques has offered new prospects to overcome these challenges. However, thermocouples and thin-film gauges remain valuable for cases where optical access is limited, very fast frequency response is required (~ 100 kHz for thin films) or for validating optical methods. Optical measurement techniques are non-intrusive (no thermal or fluid dynamic interference of a sensor with the flow) and allow the estimation of the temperature field over the entirety two-dimensional specimen surface. In this category, thermochromic liquid crystals (LC) and temperature sensitive paints (TSP) enable temperature measurements exploiting the correlation between colour changes to specific temperature values, and have been widely employed in jet engine and gas turbine research [3–5]. A limitation of these techniques is their operating temperature range, which varies with the substrate composition, and which is further constrained when a single paint is used. Although not directly providing a measure of temperature, pressure sensitive paints (PSP) have also contributed significantly to heat transfer research, particularly in the quantitative assessment of film cooling effectiveness [6–8]. All three techniques (LCs, TSPs, and PSPs) require external light sources, making the implementation in a rotating facility particularly challenging. Lastly, thermal paints, which undergo an irreversible colour change when exposed to specific threshold temperatures, offer a high temperature capability. However, they are limited to visualising peak temperatures and isothermal distributions, and the cost is often prohibitive due to their disposable nature [9].

In contrast, infrared (IR) thermography is non-intrusive, provides a high-resolution two-dimensional temperature field without requiring an external lighting source, and does not present an upper temperature limit of operation. In addition, modern IR cameras can achieve very low integration time and high frame rate, enabling measurement on objects travelling at high velocity. These aspects make infrared thermography a viable candidate to study heat transfer phenomena in the high-pressure turbine section of a rotating facility, however, particular consideration needs to be given to the calibration methodology to ensure high measurement accuracy. A review presented by Falsetti et al. [10] reports the state of the art in IR cameras and pyrometers calibration techniques, highlighting the challenges to reduce measurement uncertainties. Based on these findings, the study published by Sisti et al. [1] outlines a

calibration methodology for IR thermography measurements on fast moving targets, which is used to process the results presented in this paper.

This paper presents the first experimental results of full rotor tip heat transfer analysis using high-resolution (2D) infrared thermography. In particular, the study presents, for the first time using any measurement technique, results of adiabatic wall temperature and scaleable non-dimensional Nusselt number on a rotating turbine blade in a transonic test facility. To date, all results in literature have based non-dimensional convective heat transfer parameters on a non-scaleable reference gas temperature. The paper also analyses the effect of different camera integration times on actual turbine blades IR data collected in a rotating transonic test facility to study the trade-off between image quality, blur, and temperature measurement accuracy.

2. Literature Review

Since its introduction, the technical advancements in infrared thermography have allowed a gradual expansion of its application. With first generation infrared scanners, the capture of fast temperature transients or of temperature fields on fast-moving targets was rare. In 1997, Cardone et al. [11] used an AGEMA Thermovision 880 (8–12 μm) to quantify Nusselt numbers over a rotating disc for speeds of 576 rpm and 4,390 rpm. Given the measurement technology limitation, flow features could not be resolved, and the temperature maps were an azimuthal average. Sharp images of moving objects were only possible using the line scan feature of cameras and image reconstruction techniques, such as the approach employed by Astarita et al. [12]. The authors detected vortex formation on disc rotating up to 2,000 rpm using an AGEMA Thermovision 900 (8–12 μm). The camera acquisition frequency was reported to be 15 Hz, not enough to match the disc rotational speed, nonetheless the authors were able to detect the flow features by exploiting the line scan option of the IR scanner and reconstructing the image numerically. Temperature profiles at a single radius were acquired, displaced azimuthally by an angle function of the disc speed and line acquisition frequency. Such processing allowed the generation of a two-dimensional thermal image. Wall temperature and heat flux results of obtained without image processing by Cardone et al., and those reconstructed by Astarita et al. using 30,000 radial temperature profiles

are shown in Fig. 1(a) and (b) respectively.

From the early 2000s, studies of heat transfer on steady targets employing second generation infrared detectors, known as the staring focal plane arrays (FPAs), were published [14,15]. It was not until 2007 that the use of IR measurement techniques on rotating blades was first presented. Mori et al. [16,17] collected results of convective heat transfer measurements with a Thermosensorik CMT 348 SM IR camera featuring a 348×288 pixels mercury cadmium telluride detector. The camera was used to record the temperature at steady state conditions on the pressure side and leading edge of blades rotating at up to 1,500 rpm using an integration time of 100 μ s (frequency at full frame 150 Hz).

The application of IR thermography to rotating surfaces, specifically in rotating turbine facilities, is still limited to a few research groups. The first group to publish on this topic was the Laboratory for Energy Conversion in ETH Zurich in 2017. Lazzi Gazzini et al. [18] employed a FLIR SC7300L long-wave infrared (LWIR) camera, featuring a 256×320 pixels mercury cadmium telluride (HgCdTe or MCT) detector, cooled by a Stirling refrigerator at 77 K, to study the heat transfer on the rotor endwall in a 1.5 stage turbine steady-state facility rotating at 2,700 rpm. The authors highlighted the importance of optimising acquisition parameters for accurate heat transfer measurements, proposing an image processing approach that combined two sets of data obtained with different camera integration time: the low motion blur at 10 μ s, and the low noise at 50 μ s. The impact of frame averaging was also stated, as the superposition of 1000 frames for a single measurement was used to improve the signal-to-noise ratio in images, made possible thanks to the long duration operation mode of the facility. It is noted, the nominal rotational speed in this facility is over three times lower than the Oxford Turbine Research Facility.

In 2021, Knisely et al. [19,20] reported IR thermography surface temperature measurements in the START facility at Penn State University, a long duration facility which allows nominal speed of 10,000 rpm. The impact of integration time on blur was discussed in [19] in terms of temperature error in a simplified low speed experiment, while a qualitative comparison is made between thermal images acquired in the START facility. First on a stationary calibration, the authors showed that RMS error of calibration curve fits and spatial noise were reduced by increasing camera integration time and number of averaged frames, recommending a minimum of 50 averaged frames. This was confirmed in a simplified spin-test experiment in which a paint spot on a flat disc rotating up to 3,800 rpm was imaged, and by qualitatively comparing images of cooled blades in the START facility tested for speed up to 86% of the turbine nominal speed over a range of integration time from 1 to 10 μ s. The results confirmed the impact of averaging 100 frames in

reducing spatial noise compared to the single-frame images. The impact of integration time on blur was also studied using a nondimensional parameter d^* that quantifies the number of diameters that an object travels while the image is captured, which is in other words a nondimensional quantification of blur. By qualitatively comparing images, they concluded that integration times of 2 μ s and 3 μ s were needed at 86% blade speed to be within the range of optimal values for blur of $0.2 < d^* < 0.6$, thus achieving the best balance between motion blur and noise. This result also highlighted that there may be multiple suitable integration times for a particular speed.

Heat flux is determined in short duration facilities from measurement of the thermal transient from a known isothermal condition. By contrast, adiabatic conditions exist in steady experiments. Consequently, the approach proposed by Knisely et al. of using frame averaging to reduce spatial noise is not feasible in a short duration facility. Also, the temporal errors that arise at very low detector saturation levels, experienced at the start of the thermal transient, are considered in this paper. Measurement errors at very low detector saturation, as investigated by Sisti et al. [1], arise from the inability of the camera detector to differentiate between the internal noise and the signal level. When the incident energy strikes the detector FPA, electrons are collected over the pixel integrated capacitor which in turn collects energy for the duration of the set integration time. An analogy often used in the field is that of the buckets in the rain, at low temperature the buckets are filled at a lower rate as there are fewer photons. Thus, leading to high temporal errors at low detector saturations.

The Ohio State University (OSU) turbine research facility with nominal rotor speed of up to 13,500 rpm, also introduced IR thermography in 2021. Christensen et al. [21] implemented an IR camera to capture images of surface temperature on a small region of the turbine blade tip. The study highlighted the critical role of integration time in balancing motion blur and image noise in high-speed infrared measurements of turbine blades. After conducting preliminary experiments, a factory-calibrated integration time of 47.6 μ s was selected as an optimal trade-off, still resulting in significant motion blur. A small portion of the cooled blade tip was imaged and a deblurring algorithm was employed in post-processing to correct the blurred images. In a subsequent work [22], the data was used alongside numerical simulations to examine the performance of blade tip film cooling. Experimental infrared data and the numerical conjugate heat transfer predictions of spatially averaged temperatures were found in agreement within 0.6%, demonstrating the capability of the IR measurement system to capture low spatial frequency temperature distributions.

Since the short duration operating conditions are more similar to the

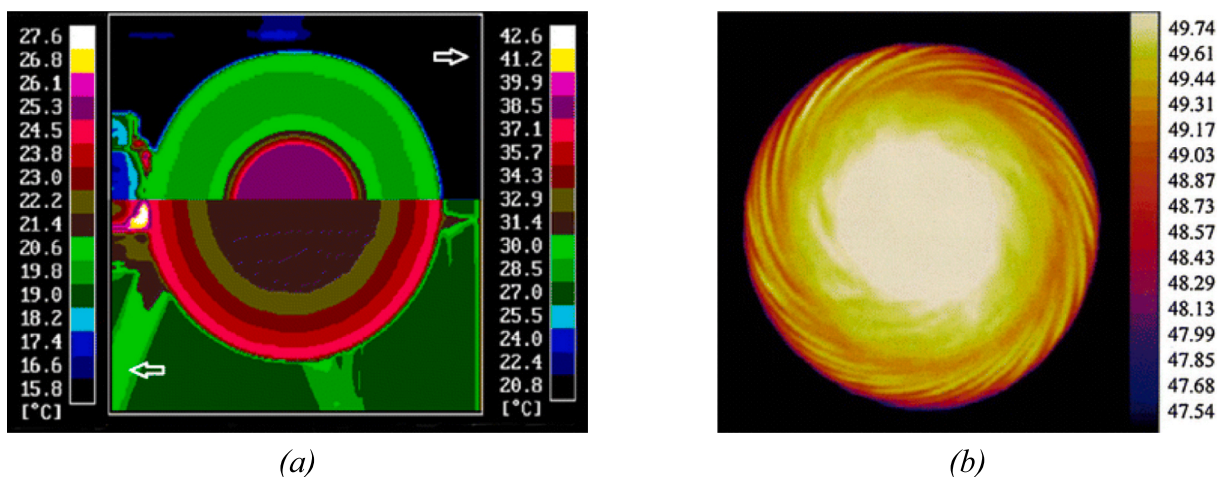


Fig. 1. (a) 450 mm disk rotating at 4,390 rpm. Upper half (right scale) wall temperature for a Joule heat flux of 871 W/m^2 . Lower half (left scale) wall temperature for a with a Joule heat flux of 0 W/m^2 (adapted from [11]), (b) Reconstruction of spiral vortices on a rotating disk (adapted from Astarita et al. [12]). Images were collected from the review by Carlomagno and Cardone [13].

OTRF, the measurement developments from Ohio State University are more relevant to the present study. In comparison, the OTRF offers a larger infrared transparent window for optical access allowing capture of up to four blade tips in a single image. Furthermore, like all historic rotor heat transfer studies in such test facilities, convective heat flux measurements are referenced to a gas temperature rather than adiabatic wall temperature, resulting in Stanton number that cannot be directly scaled to engine conditions. In contrast, the measurement system presented in this paper allows full spatially resolved measurements of adiabatic wall temperature and scaleable Nusselt number on a turbine rotor tip obtained with IR thermography in a rotating facility at engine matched conditions.

More recently, Anthony et al. [23,24] investigated the application of thermal imaging techniques at the AFRL Turbine Research Facility (TRF), a short-duration, full-scale turbine test rig operating at rotational speeds up to 7,400 rpm with approximately 2 s of hot gas flow. The first study [23] presented a preliminary investigation of the thermal imaging system employing a commercial long-wave infrared (LWIR) camera integrated with custom made optical probes. The focus was on developing data acquisition workflows, blade image synchronisation, and position triggering methods. The capability to synchronise the thermal camera to a specific blade position during rotation, enabling repeatable imaging of the blade pressure surface leading edge, trailing edge, and suction surface leading edge, including platform regions was demonstrated.

Showing a thermal image of the blade pressure side leading edge, constructed by averaging 60 frames over the blowdown duration, the authors demonstrated the system's qualitative ability to capture the blade main features. However, the transient nature of the test prevented using conventional signal-to-noise improvement methods, such as averaging hundreds of frames at a steady-state point, as suggested by Knisely et al. [19]. Instead, the authors explored the impact of spatial averaging across small regions of interest (ROIs) to reduce random noise. They found that for a 13×13 pixels ROI, averaging as few as 3 to 6 frames significantly improved signal quality, thus reducing the reliance on extensive temporal averaging typical in single-pixel analysis (it should be noted, however, that this approach comes at the cost of reduced spatial resolution). Finally, the study presented temperature time histories (without temporal averaging) at a fixed location on the blade pressure side across the full 2 s test duration.

In the second study, Anthony et al. [24] presented calibrated temperature measurements from the same test rig. Calibration was performed using the Planck blackbody equation, with background corrections applied by subtracting background images obtained by closing the camera shutter close in time to the measurements. Image quality was evaluated by comparing data collected at integration times of 4 μ s and 5 μ s at 7,500 rpm, and at 200 μ s under static conditions (baseline), although the baseline does not appear to be captured under the same viewing conditions as the rotating images. The comparison highlighted that the 5 μ s images offered good radial resolution, while exhibiting motion blur in the circumferential direction. On the other hand, the 4 μ s images had lower signal-to-noise ratios but improved clarity of small-scale features circumferentially. Thermal images, presented as temperature maps (in Fahrenheit), were used to identify off-design phenomena such as transient hot gas ingestion and subsurface blocked cooling passages.

Despite advancements in infrared thermography for studying rotating turbine blades, challenges remain in capturing high-quality thermal images under high-speed rotating conditions and in determining the parameters impacting the accuracy of IR images. While previous studies have optimised integration time and used deblurring algorithms to reduce motion blur, these methods do not fully address the impact of integration time at higher speeds in transient tests. This study aims at addressing this gap by investigating the optimal integration time for accurate infrared imaging of turbine blades at higher rotational speeds in a short duration turbine test facility. It demonstrates the capability of infrared thermography to capture temperature and heat

transfer phenomena in gas turbine research, emphasizing the significant impact of camera integration time on image quality and temperature measurement accuracy. It also presents an evaluation of the impact of integration time and blur on the heat transfer analysis, in particular studying this impact on adiabatic wall temperature and Nusselt number for the first time in literature.

3. Experimental Setup

Experiments were conducted in the Oxford Turbine Research Facility (OTRF), a short-duration light piston tube facility of engine scale developed for turbine aerodynamics and heat transfer investigations. The facility is capable of testing fully film-cooled high-pressure turbine stages, with or without an intermediate pressure or low-pressure stator, at engine representative Mach and Reynolds numbers, non-dimensional speed and gas-to-wall temperature ratio. Furthermore, a novel combustor simulator can be used to generate two-dimensional profiles of temperature and velocity at the turbine inlet representative of both rich and lean burn combustors [25]. A summary of recent research conducted in the facility is presented in Falsetti et al. [26].

A schematic of the OTRF and a representation of the infrared thermography setup are shown in Fig. 2. Depicted in Fig. 2(a), the facility consists of four main sections: the pump-tube enclosing a lightweight piston, a fast-acting plug valve, the working section (which houses the test turbine) and a large exhaust tank. Prior to a test, the plug valve is closed isolating the pump tube and working section. Air is evacuated from the working section and exhaust tank to a vacuum level of approximately 10 mbar; this condition enables the turbine rotor to be spun by an air motor minimising windage losses and heating. Once the turbine has been spun to the desired speed, high pressure air is injected behind the free piston that travels down the piston tube, thereby isentropically compressing the test gas in front of the piston. When the desired stagnation temperature and pressure inlet conditions are achieved, the fast-acting valve is opened to allow the hot gas to flow into the test section. The infrared thermography setup illustrated in Fig. 2(b) comprised an IR transparent window for optical access, IR camera, and camera mounting. With a camera working distance of approximately 125 mm, each thermal image captured two blade passages, while the mounting system enabled alignment of the camera to capture the blade tip, pressure, and suction sides.

The camera used in this study was a FLIR A6751 LWIR, chosen for its sensitivity in the temperature range of interest and detector speed. The camera features a 640×512 pixels Focal Plane Array (FPA) and cooled Strained Layer Superlattice (SLS) detector, sensitive to the long wavelength infrared range, which suits the expected experimental peak emission of 9 μ m approximately. As the IR camera features a working wavelength of 7.5 – 11 μ m, an optical material with a long wave infrared transmission band was required. Possible candidates of materials transmitting in the LWIR range are: zinc sulphide (ZnS), gallium arsenide (GaAs), zinc selenide (ZnSe), and germanium (Ge) [27]. Ultimately, zinc selenide was chosen as its transmissivity is a weak function of temperature and has good mechanical properties. More details on the thermography set-up can be found in Sisti et al. [1].

Time traces of stage inlet total pressures and temperature, total-to-static pressure ratio, and rotor speed for a typical run with uniform inlet conditions are shown in Fig. 3. Vacuum and ambient temperature are the conditions at the beginning of the test. The cooling flows are injected prior to the opening of the plug valve, and can be seen in the pressure and temperature traces by a rise at $t = 1.9$ s. The consequent rise in total temperature is a result of isentropic compression of the working section air. At $t = 2.43$ s the fast-acting plug valve opens and the inlet total pressure and temperature increase. At $t = 2.60$ s, inlet total pressure and total temperature reach quasi-steady conditions, with mean values equal to the nominal design condition ($p_{01} = 5.4$ bar; $T_{01} = 475$ K). The test run ends when the piston reaches the end of the piston tube at $t = 2.92$ s. The rotor nominal speed of 8,500 rpm is achieved to

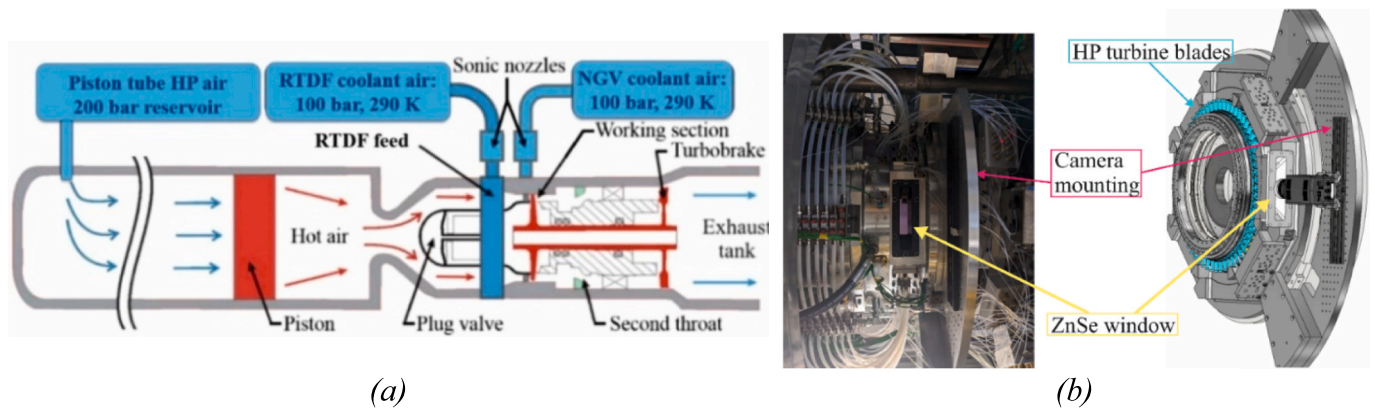


Fig. 2. (a) Schematic of OTRF; (b) Infrared thermography setup, showing a photograph and 3D model of turbine working section ([1]). Adapted from [1].

within ± 20 rpm during the stable portion of the run, which lasts approximately 0.3–0.5 s. In Fig. 3, the pressure and temperature stable regions are individuated by black dashed and red solid vertical lines, respectively. The run start and finish are defined by the interval where the two regions overlap.

The turbine investigated in this study was a Strategic Investment in Low-Carbon Engine Technology (SILOET) turbine, which features 40 HP vanes with surface film cooling and trailing edge slot ejection, 60 transonic HP rotor blades, designed with 50% reaction [28]. The operating conditions of the SILOET turbine in the OTRF with permissible run-to-run variability are summarised in Table 1.

Infrared thermography was used to measure surface temperature and the impulse response method [29] was employed to compute heat flux. In a transient test facility, the accuracy of the method, as well as the successful regression to heat flux and surface temperature to obtain adiabatic wall temperature, rely on an appreciable temperature rise within the stable portion of the experiment. This is only possible using a substrate manifesting low thermal conductivity. Hence, the rotor blades were coated with PolyEtherEtherKetone (PEEK) to implement full surface IR thermography measurements. As a fully plastic blade would not survive the centrifugal loads in the facility, a metallic insert was coated with PEEK. The manufacturing process (shown in Fig. 4) included CNC machining of the blade insert, injection moulding of the plastic coating, and final CNC machining of the blade geometry. As the impulse response method relies on a semi-infinite substrate assumption, analysis of thermal penetration depth is required. The penetration depth of a thermal pulse into a substrate can be approximated by $x = 4\sqrt{\alpha t}$ [30]. For a PEEK substrate with thermal diffusivity $\alpha = 0.158 \text{ mm}^2 \text{ s}^{-1}$ at 80°C and test duration of $t = 0.5 \text{ s}$, a minimum substrate depth of 1.12 mm is required to satisfy the semi-infinite substrate assumption, an order of magnitude lower than minimum thickness of 2 mm on the composite blade tip. In the rotor assembly, a total of 14 out of 60 blades were coated with PEEK and allocated for IR thermography measurements. Infrared measurements concentrated on the blade tip region, which featured a double-sided squealer tip with an open trailing edge (see Fig. 4, right-hand photograph), with aerodynamic results presented by Singh et al. [31].

The IR camera was synchronised to the blade rotation, thus working at a framerate equivalent to the rotor passing frequency and capturing one image per revolution. The camera framerate at full window of 125 Hz was increased by windowing down the field of view to match the expected rotor frequencies of 130–142 Hz. To maximise the field of view, an image size of 624×364 pixels was selected allowing a maximum framerate of 178 Hz. The camera synchronisation and triggering was achieved using a National Instruments sRIO FPGA digital inputs/outputs operating at 40 MHz. The shaft speed and blade passing signals enabled blade counting and generation of the camera

synchronisation signal, based upon the user selected blade number. The possibility to delay the synchronisation signal as a percentage of measured phase difference between adjacent blade passage was also implemented, enabling control over blade positioning in the field of view.

A summary of testing conditions is shown in Table 2.

4. Data Processing

4.1. Image processing to obtain target temperature maps

The IR thermal data presented in this study was processed following the calibration and processing methodology described in Sisti et al. [1]. The detector calibration, as well as emissivity and transmittance calibrations, were conducted ex situ given the unfeasibility of achieving accurately known temperatures up to 500 K on a calibration blade in a large scale, metallic, rotating facility.

Infrared data in the OTRF was recorded in the form of raw digital counts and converted to blackbody equivalent temperature, T_{cam} , using the detector calibration curves shown in Fig. 5. The IR camera detector calibration was conducted ex situ against traceable blackbodies (CI-Systems SR33-7 for temperatures below 350 K and Fluke 418 for temperatures above 350 K, chosen for the better accuracy each calibrator offers in the specific temperature range [1]) and performed over a range of temperature relevant for the study carried out in the OTRF, from 293 K to 543 K, for different integration time values.

The total spectral radiance reaching the infrared detector is not solely the one emitted by the target. Instead it includes multiple radiative contributions, including the energy emitted by the target, the energy from surrounding surfaces that is reflected by the target, and the energy emitted by the optical path between the target and the detector. The energy balance, rearranged using the Stefan-Boltzmann equation, can be written as:

$$T_{cam}^4 = \tau \epsilon T_t^4 + \tau(1 - \epsilon) T_r^4 + (1 - \tau) T_{opt}^4 \quad (1)$$

where T_{cam} is the blackbody equivalent temperature measured by the detector, T_t is the true target temperature, ϵ is the target emissivity, T_r is the reflected temperature representing surrounding radiative sources, τ and T_{opt} are the equivalent transmittance and temperature of the optical path, respectively. Thus, accurate measurement of T_t requires knowledge of ϵ , T_r , τ , and T_{opt} , as each term accounts for energy contributions from the target, reflected environment, and optical path, which need to be calibrated, measured, or calculated.

In this study, the target emissivity was calibrated ex situ [1]. For the optical path contribution, knowing the transmissivity of air can be considered unity [32], the equivalent optical path transmissivity and temperature could be considered for the optical window alone. A

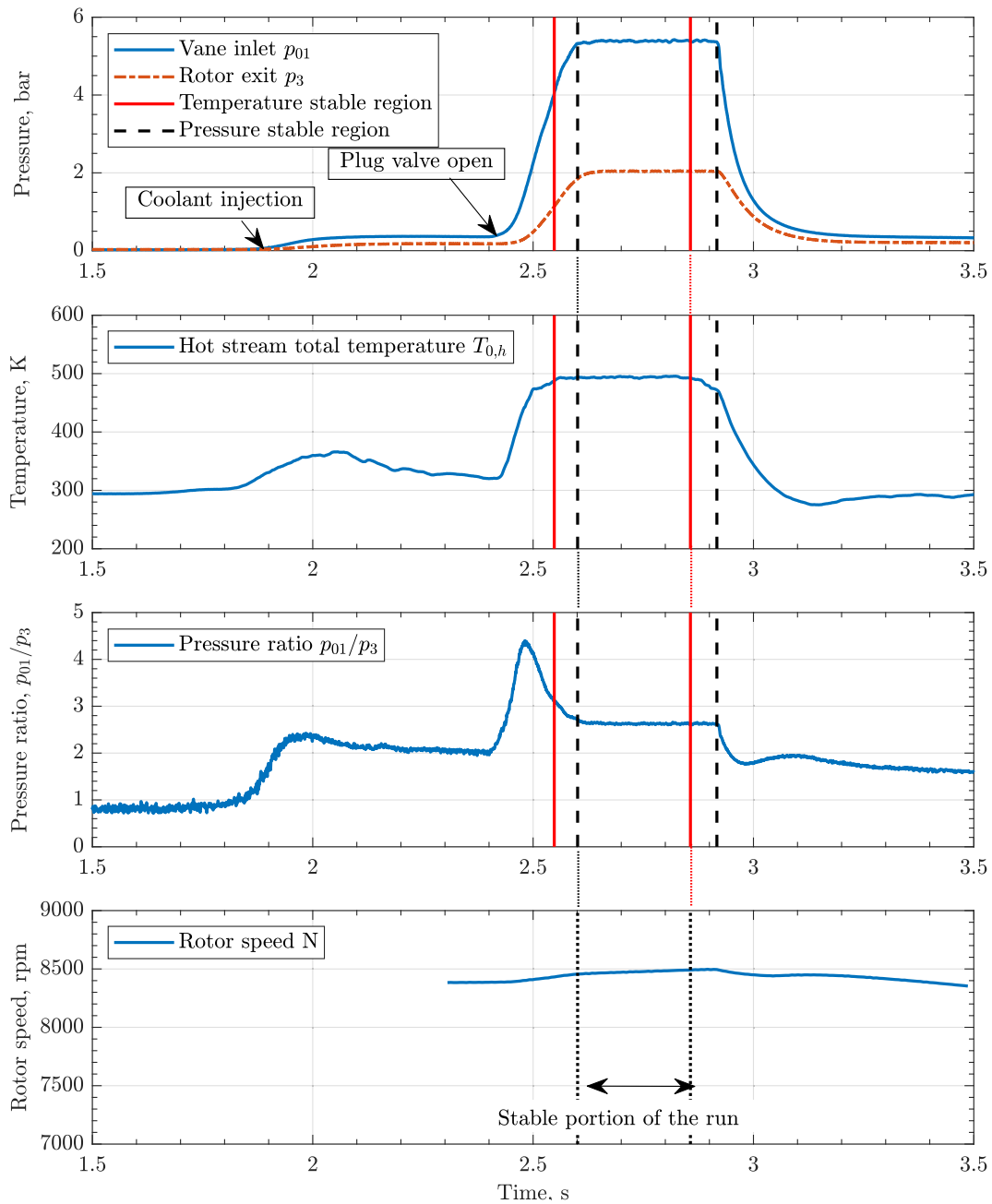


Fig. 3. Typical traces of stage pressure and temperatures for an OTRF run with uniform inlet conditions. Rotor speed is also shown.

Table 1
SILOET turbine design conditions in the OTRF.

Parameter	Symbol	Nominal value	Run-to-run variability
Vane inlet total pressure	p_{01} (bar)	5.4	$\pm 1\%$
Vane inlet total temperature	T_{01} (K)	475	$\pm 2\%$
Rotor exit static pressure	p_{03} (bar)	2.05	–
Stage total-to-static pressure ratio	p_{01}/p_{03}	2.63	$\pm 2\%$
Speed	N (rpm)	8500	$\pm 1\%$
Corrected speed	$N/\sqrt{T_{01}}$ (rpm/K)	390	$\pm 1\%$

transient heat convection model was conducted on the optical window geometry with representative (though worst case) experimental boundary conditions: internal air temperature $T_{int} = 475$ K; external air temperature $T_{ext} = 295$ K; internal heat transfer coefficient $h_{int} = 2000$ $W\ m^{-1}\ K^{-1}$, and external heat transfer coefficient $h_{ext} = 0$ $W\ m^{-1}\ K^{-1}$. Given the short duration of the OTRF test of 0.5 s and the window material properties [33], results indicated that the temperature of the external window surface increased less than 1 K. The internal surface temperature increased by approximately 7 K with a thermal pulse depth of $\sim 2\%$ minimum window thickness. Hence, the equivalent optical path temperature (i.e. the window temperature) could be considered equal to ambient conditions, and a measure of ambient temperature during the run was used for the optical path temperature corrections. The transmissivity of the zinc selenide window used in the experiments was calibrated ex situ at ambient conditions and measured at 0.95 ± 0.02 [1].

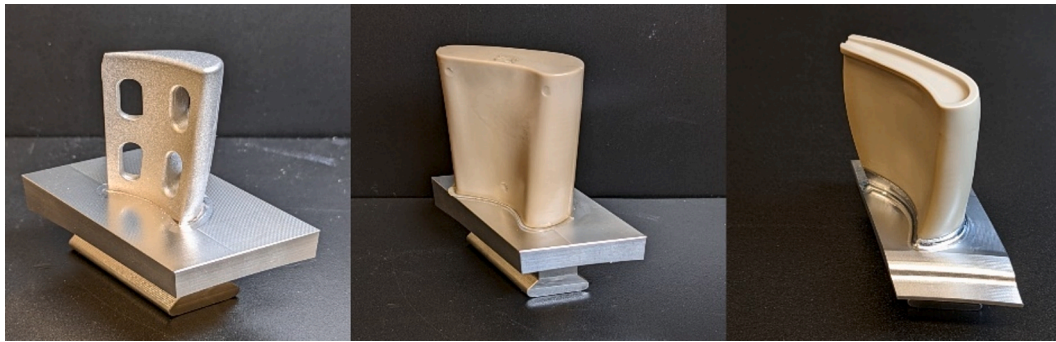


Fig. 4. Photographs of composite blade insert (left), moulding (middle) and final machining (right).

Table 2
Conditions for IR thermography rotor tip heat transfer measurements in the OTRF.

Blades	IR blades coated with PEEK and spray painted	14
	Nominal geometry blades	46
Rotor	Nominal rotational speed	8500 rpm
	Tip radius	0.296 m
	Nominal absolute velocity	263.5 ms ⁻¹
	Speed range during testing	8350–8500 rpm
	Nominal rotor frequency	142 Hz
	Frequency range during testingNominal blade passing frequency	130–142 Hz 8520 Hz
Temperature	Gas temperature at NGV inlet during testing*	475 K
Camera	Model	FLIR A6750 SLS
	Framerate**	130–142 Hz
	Integration time	20, 10, 5, 2, 1 μs
	Working distance	~125 mm
IR dataset***	Frames	~630 frames
	Seconds	~4.5 s
Scene	Pixels	624 x 364
	Geometrical	2.5 blade tips
Window	Material	Zinc selenide

* Measured by radial rakes of k-type 25.4 μm diameter bare-bead thermocouples.

** Camera synchronized to rotor frequency.

*** One frame/image captured per revolution.

Lastly, correction for surrounding reflections (i.e. the reflected temperature) was achieved combining two datasets with differing surface emissivity acquired from two experimental tests with the same aerothermal field and viewing angle conditions. The first test, focussed on a blade coated with high emissivity Nextel velvet black in the centre of the Field of View (FOV), the second on a blade coated with Ambersil aluminium in the centre of the FOV. This was made possible by the IR camera synchronisation system, which allowed the image acquisition to be triggered according to the desired blade location. The two FOVs are shown in Fig. 6, where a red dashed line encompasses the blade of interest: blade 1 – subscript 1, high emissivity, ϵ_1 , and blade 2 – subscript 2, low emissivity, ϵ_2 . The emissivity values of the two paints were found through a traceable calibration to an uncertainty of ± 0.01 [1], providing values of 0.97 for the Nextel velvet black paint and 0.6 for the Ambersil aluminium paint.

A system of two equations in two unknowns stems from the IR energy

balance Eq. (1), that can be solved to obtain the corrected target temperature and the reflected temperature as expressed below:

$$T_t^4 = \frac{1 - \epsilon_2}{\tau(\epsilon_1 - \epsilon_2)} T_{cam1}^4 - \frac{1 - \epsilon_1}{\tau(\epsilon_1 - \epsilon_2)} T_{cam2}^4 - \frac{\tau}{1 - \tau} T_{opt}^4 \quad (1)$$

$$T_r^4 = \frac{\epsilon_1}{\tau(\epsilon_1 - \epsilon_2)} T_{cam2}^4 - \frac{\epsilon_2}{\tau(\epsilon_1 - \epsilon_2)} T_{cam1}^4 - \frac{\tau}{1 - \tau} T_{opt}^4 \quad (2)$$

A block diagram summarising the data analysis workflow from raw digital counts to target temperature is shown in Fig. 7.

4.2. Visualisation of run phases

Fig. 8 illustrates the temporal evolution of the blackbody equivalent temperature T_{cam1} during various stages of the test run (marked A, B, C & D). Positioned at the top are infrared images capturing the blade, with a specific pixel on the blade tip marked by a starshaped marker. Beneath the infrared images, a plot displays the temporal history of T_{cam1} corresponding to the highlighted pixel. One frame was chosen for each stage.

During stage A ($0 < t < 1.5$ s), the rotor is spinning in near vacuum (10 mbar), causing slight frictional heating on the blade tip. During this phase, T_{cam1} shows a slightly elevated temperature from ambient conditions (298 K) by ~ 14 K on the squealer rim and ~ 7 K in the tip gutter. The remainder of the facility remains at near ambient conditions, hence, little contrast is seen between the facility components.

During stage B ($1.5 < t < 2.4$ s), ambient temperature coolant flows are initiated and stabilised. This cools the blade back to near ambient and isothermal conditions. Horizontal stripes of lower temperature on the blade tip result from an arrangement of discrete cooling holes situated on the static casing above the rotor tip. During this phase, the cooling flow from the casing impinges on the rotor tip. This demonstrates the sensitivity of the measurement, clearly detecting only a few degrees of temperature difference.

Stage C is the main test period. At $t = 2.4$ s, the facility plug-valve opens allowing hot test gas to flow through the turbine test section until $t = 2.9$ s when the main test period ends. The blade temperature increases during the test period, with T_{cam1} on the blade tip reaching approximately 400 K. This portion of the run presents IR images that are sharp with the best contrast levels, and some qualitative observation can be drawn from the image. All three blades tip, pressure, and suction surface are composite in construction and exposed to the same temperature field, so it is reasonable to conclude they are at the same temperature, however, they are coated with paints of different emissivity (see Fig. 6). The central blade, with $\epsilon = 0.97$, provides an equivalent blackbody ($\epsilon = 1$) temperature close to the true target temperature, whilst the two neighbouring blades, $\epsilon = 0.60$, record a much lower equivalent blackbody temperature, as expected. Although the central blade platform is coated with high emissivity paint, the substrate is aluminium rather than PEEK (see Fig. 4). Subsequently, the

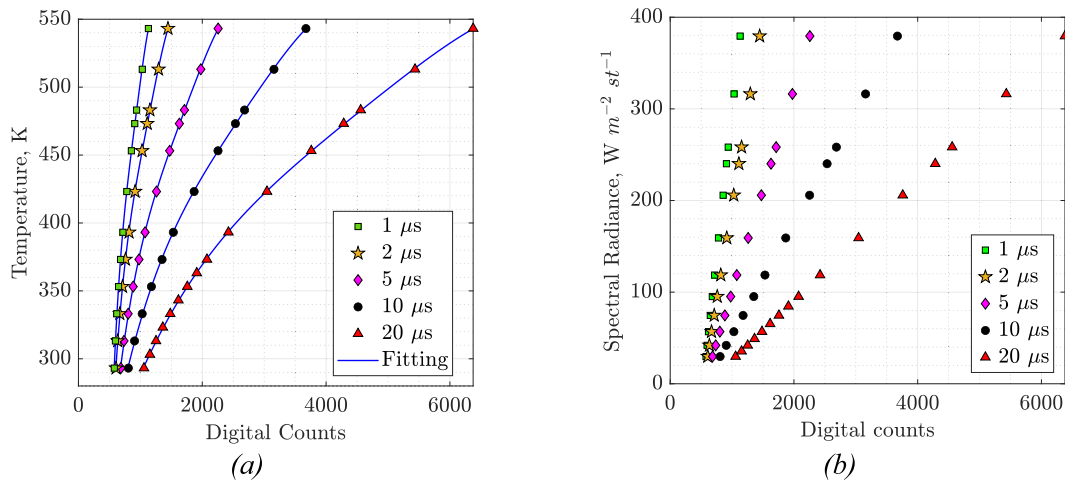


Fig. 5. Camera detector calibration for integration times of 20, 10, 5, 2, and 1 μs in terms of (a) Equivalent blackbody temperature and (b) Radiance as a function of digital counts.

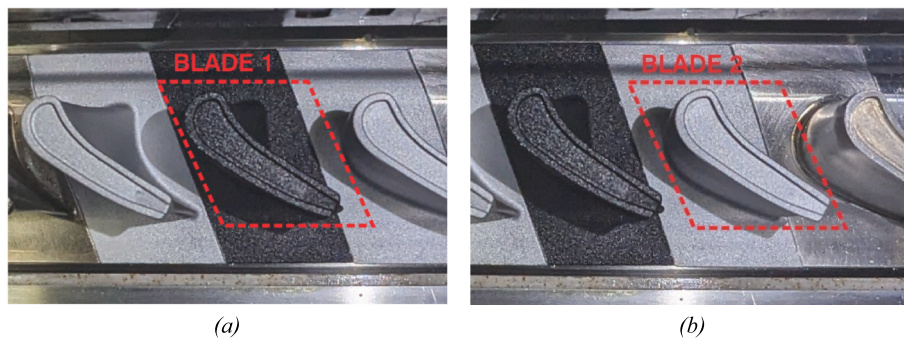


Fig. 6. Photographs of (a) FOV 1 and (b) FOV 2 with highlighted blades of interest.

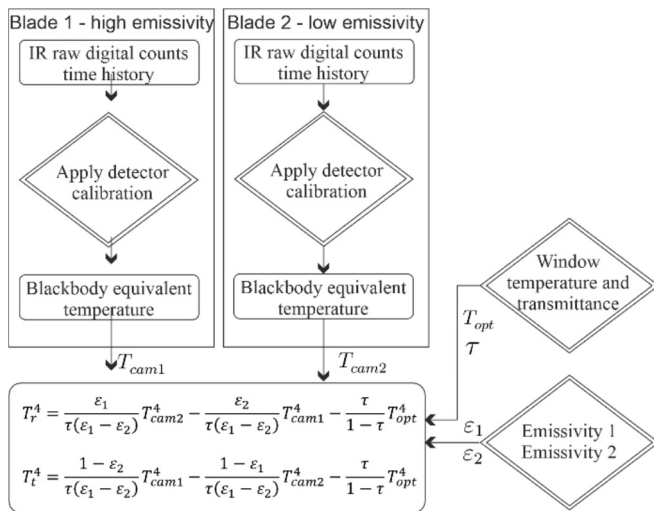


Fig. 7. Infrared thermography data analysis workflow.

platform surface temperature is lower due to a significantly higher substrate thermal product. Maximising the surface temperature rise during experiment is important to minimise errors in time resolved surface heat flux, hence the motivation for the composite blade design.

Finally, in Stage D after $t = 2.9$ s, the supply of hot test gas ends and the rotor spins down. The sudden reduction in facility pressure causes a near isentropic reduction of the gas temperature within the facility,

resulting in a reduction of all surface temperatures. Once the facility pressure has stabilised ($t \sim 3.6$ s), the facility remains at approximately 100 mbar causing frictional heating on the blade again.

4.3. Infrared data and corrections

Infrared thermal images of a blade tip for a single frame (number 392) acquired during the steady test period under engine-representative conditions (8,500 rpm, $T_{0,in} = 475$ K) are shown in Fig. 9(a)-(d) for an integration time of 5 μs. Processed data is shown for blackbody equivalent temperatures for each blade, T_{cam1} (actual $\epsilon = 0.97$) and T_{cam2} (actual $\epsilon = 0.60$), corrected target temperature, T_t , and reflected temperature, T_r . Fig. 9(e) plots the variation of these temperatures against time, for a single pixel located in the blade tip gutter towards the leading edge. The thermal images show a distinct image of the blade tip, which is moving at ~ 265 ms⁻¹ from right to left in this view, with slight blur (~ 12 pixels at the tip plane). The squealer rim geometry (thickness of ~ 1.3 mm) is also visible.

During rotor spin up (time 0 to ~ 1.5 s), T_r remains at near ambient conditions of 295 K, which is comparable to T_{cam2} exhibiting 300 K, whilst T_{cam1} and T_t show a slightly elevated temperature by ~ 7 K as expected due to frictional heating of the blade tip. As ambient temperature cooling flows are initiated and stabilised, T_{cam1} and T_t return to near ambient conditions and close to T_r and T_{cam2} (time 1.5 s–2.4 s). As hot test gas flows through the turbine test section at $t = 2.4$ s, T_{cam1} , T_{cam2} , T_t and T_r all increase during the test period, reaching maximum values of approximately 400 K, 378 K, 405 K and 330 K, respectively. The difference between the blackbody equivalent temperature T_{cam1} (actual $\epsilon = 0.97$) and target temperature T_t provides the combined

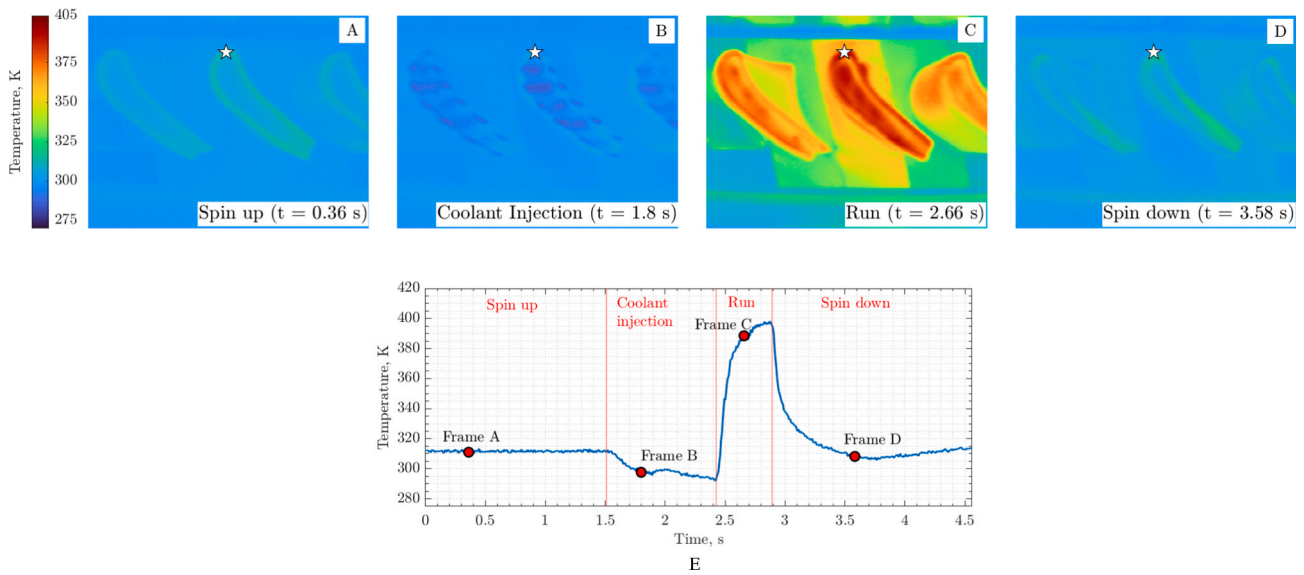


Fig. 8. Evolution of the blackbody equivalent temperature during different stages of a test run. Top: Infrared images with a single pixel marked on the blade tip. Bottom: Temporal history plot for the highlighted single pixel.

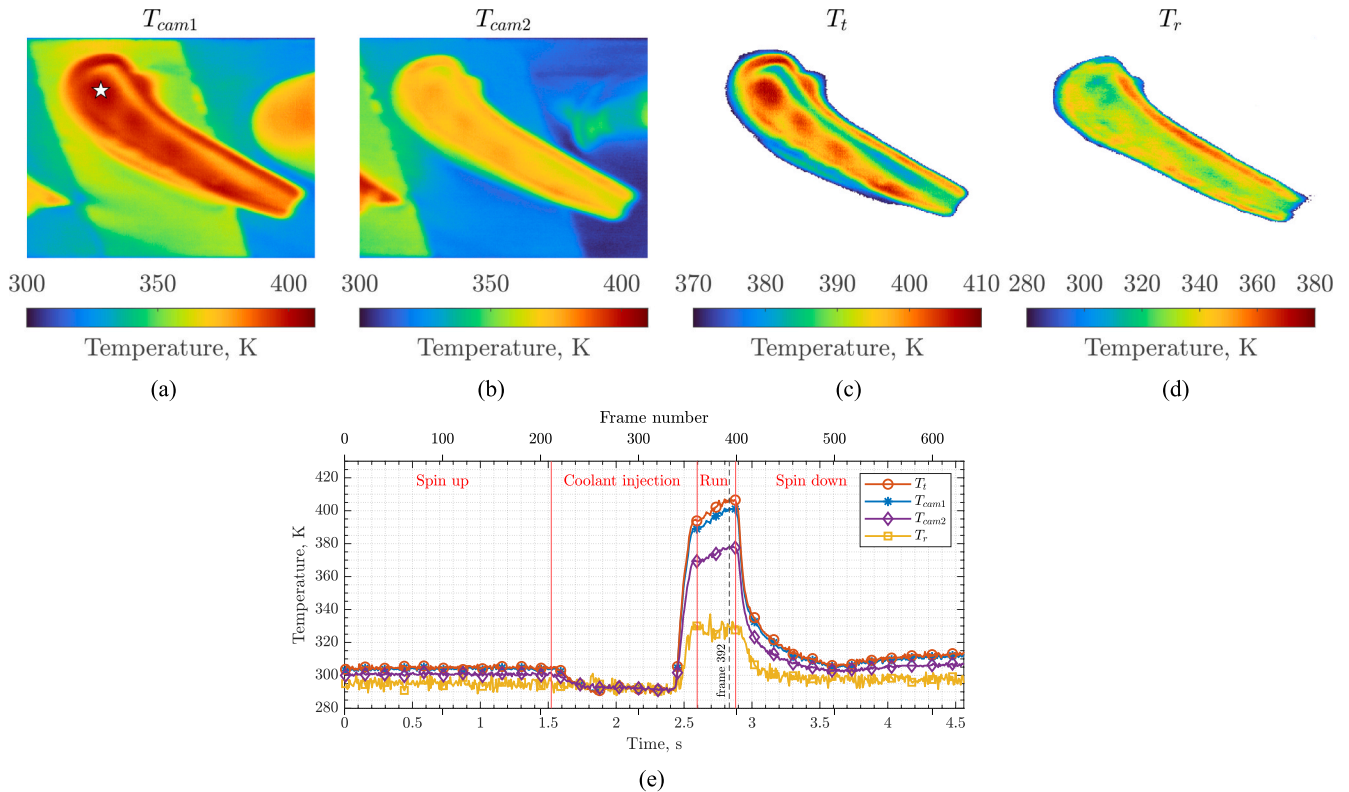


Fig. 9. Characteristic results and correction of blade tip IR thermal data captured in the OTRF. Thermal maps during the steady test period: (a), (b) blackbody equivalent T_{cam1} & T_{cam2} , (c), (d) target and reflected temperature maps; (e) time traces for single pixel as marked with a star.

correction magnitude as a function of time. The correction increases from almost zero at near ambient conditions to approximately +5 K, or +1.23%, at the end of the main test period when T_{cam1} 400 K. At the point of maximum correction, the contributions are as follows: surface emissivity correction is approximately +3.05 K (or +0.75% of T_t), optical path transmissivity correction is approximately +5.2 K (or +1.28% of T_t), surface reflections correction is about -1.35 K (or -0.33% of T_t), and correction for the optical path temperature is -1.52 K (or -0.37% of T_t). The thermal images depicted in Fig. 9 were captured with an

integration time of 5 μ s. However, the integration time significantly affects temperature measurements and their accuracy. The following sections examine its impact on measurement reliability.

5. Impact of Camera Integration Time on Blackbody Equivalent Temperature

The extent of image blur, of particular significance when capturing fast moving targets, is dependent upon both the target speed and the

chosen integration time of the camera detector. The blur level is reduced as the integration time is shortened; however, a short integration time leads to increased error and noise. Looking at the detector calibration curves in Fig. 5, it can be seen that operating at low integration times can result in higher curve fitting errors at low target temperature due to the lower detector saturation. Furthermore, lower detector saturation leads to higher temporal errors. The temporal error in the detector [1] was evaluated using a blackbody source at known temperature in equilibrium conditions. This error was quantified collecting 100 sequential frames at 125 Hz, applying the detector calibration to the measured digital counts, and computing the maximum deviation between the measured temperature and the true blackbody temperature. This error is plotted for a randomly selected pixel in the camera Focal Plane Array (FPA) in Fig. 10 as a function of integration time IT and blackbody temperature T_{bb} . At very low integration times and low blackbody temperatures, fewer photons are collected by the sensing element of the FPA (pixel). Thus, the detector is unable to distinguish between noise level and signal level, leading to higher detector temporal errors.

The detector temporal error can also be visualised in terms of the detector saturation, as depicted in Fig. 11, defined as the value recorded by the pixel, expressed in digital counts, as percentage of the camera 14-bit dynamic range. Agreeing that 2 K is an acceptable error, the interception of the constant error line at 2 K with the data show that a minimum 5% detector saturation is required.

Table 3 details the estimated blur on the blade tip expected at nominal speed conditions in the OTRF, for integration times varying from 20 μs down to 1 μs . At the nominal rotational speed of 8,500 rpm, a tangential velocity at the blade tip of 263.5 ms^{-1} is expected. Given an integration time (IT), a simple estimate of blur level in mm can be obtained as $\text{blur} = v_t \times \text{IT}$, while to convert this value in pixel the pixel-to-mm ratio can be used. For the camera working distance of 125 mm between the camera lens and the blade tip, the pixel-to-mm ratio is approximately 9.067. A nondimensional quantification of blur is given by the parameter d^* [19], defined as $d^* = \text{blur}/d$, where d is the characteristic dimension of the feature to be resolved. This parameter represents the distance an object moves, expressed in units of d , during the camera integration time. An ideal range for d^* can be defined between $d^* = 0$, representing a no-blur scenario, and $d^* = 1.2$, indicating a blur magnitude equal to 1.2 times the characteristic dimension of the feature being resolved. To resolve the width of the squealer rim around the blade tip (~ 1.3 mm), the analysis suggest that an integration time of 5 μs would be sufficient, yielding $d^* = 1$. For a typical cooling hole on a cooled blade (~ 0.3 mm in diameter), an integration time of 1 μs is required to achieve $d^* = 0.88$. If a longer integration time is used,

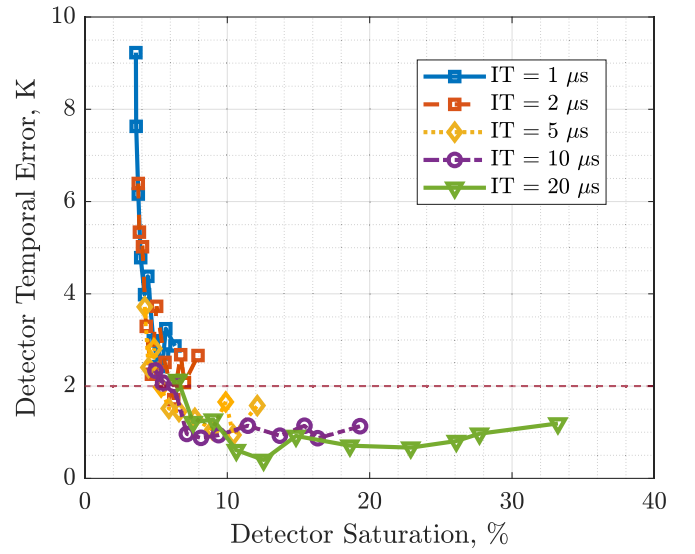


Fig. 11. Maximum absolute temporal error in T_{cam} from a randomly selected pixel shown as a function of camera detector saturation and camera integration time.

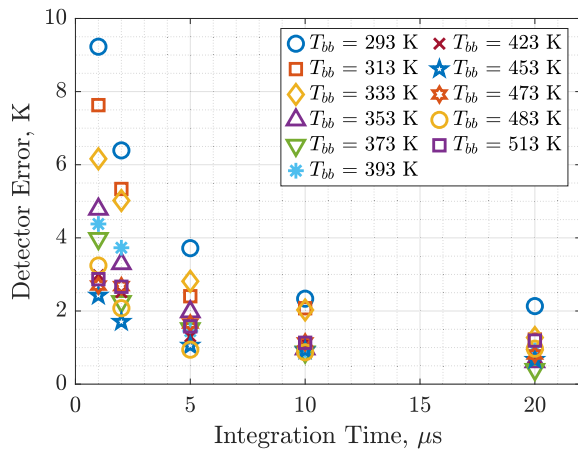
Table 3

Blur levels as a function of integration time at 8,500 rpm (target speed = 263.5 ms^{-1}).

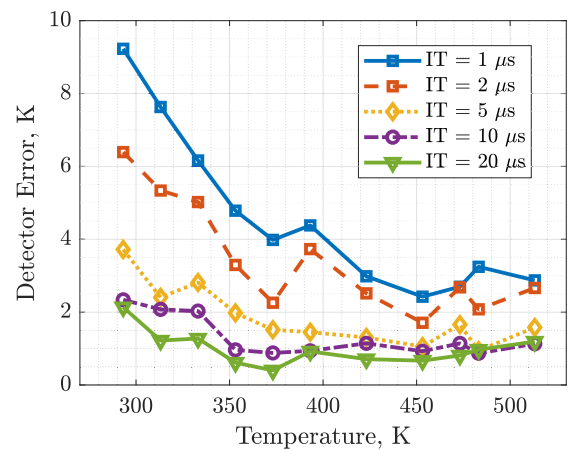
IT	μs	20	10	5	2	1
Blur	mm	5.27	2.63	1.32	0.53	0.26
Blur	pixel	47.78	23.89	11.94	4.78	2.39
d_{rim}^*	–	4.05	2.03	1	0.4	0.2
d_{holes}^*	–	17.6	8.78	4.39	1.76	0.88

additional image deblurring becomes necessary [21].

The effect of integration time on IR thermography data acquired in the OTRF was investigated comparing results from different runs under identical turbine operating conditions (consult Table 1 for run-to-run variability) and camera triggering settings. Data was collected using a range of integration time: 20, 10, 5, 2, and 1 μs . Fig. 12 presents a summary of this analysis. In Fig. 12(a), infrared images of equivalent blackbody temperature T_{cam1} are shown for a single frame selected from the stable period of each run. From top to bottom, integration time decreases from 20 μs to 1 μs . A vertical black dashed line provides a



(a)



(b)

Fig. 10. Maximum absolute temporal error in T_{cam} from a randomly selected pixel, shown as a function camera integration time and blackbody temperature. Two visualisations are proposed: (a) error versus integration time; (b) error versus temperature.

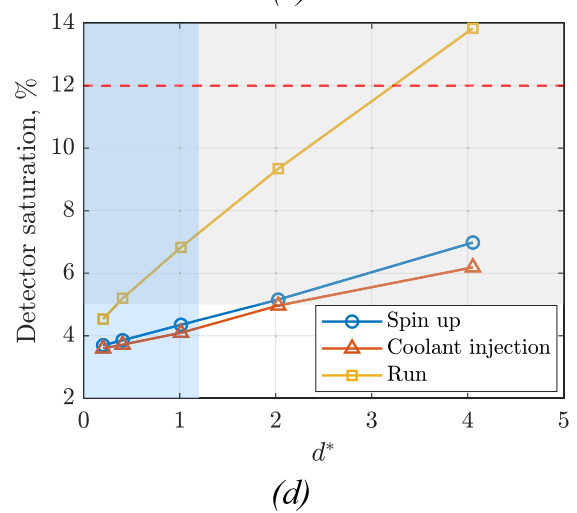
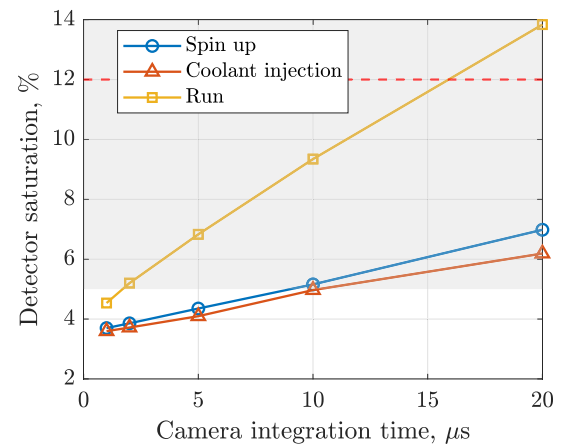
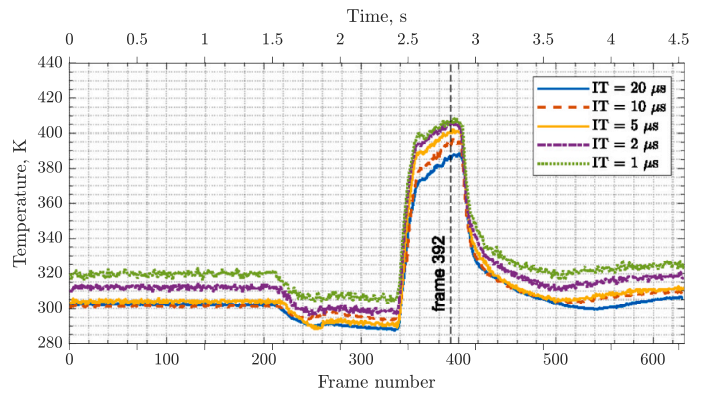
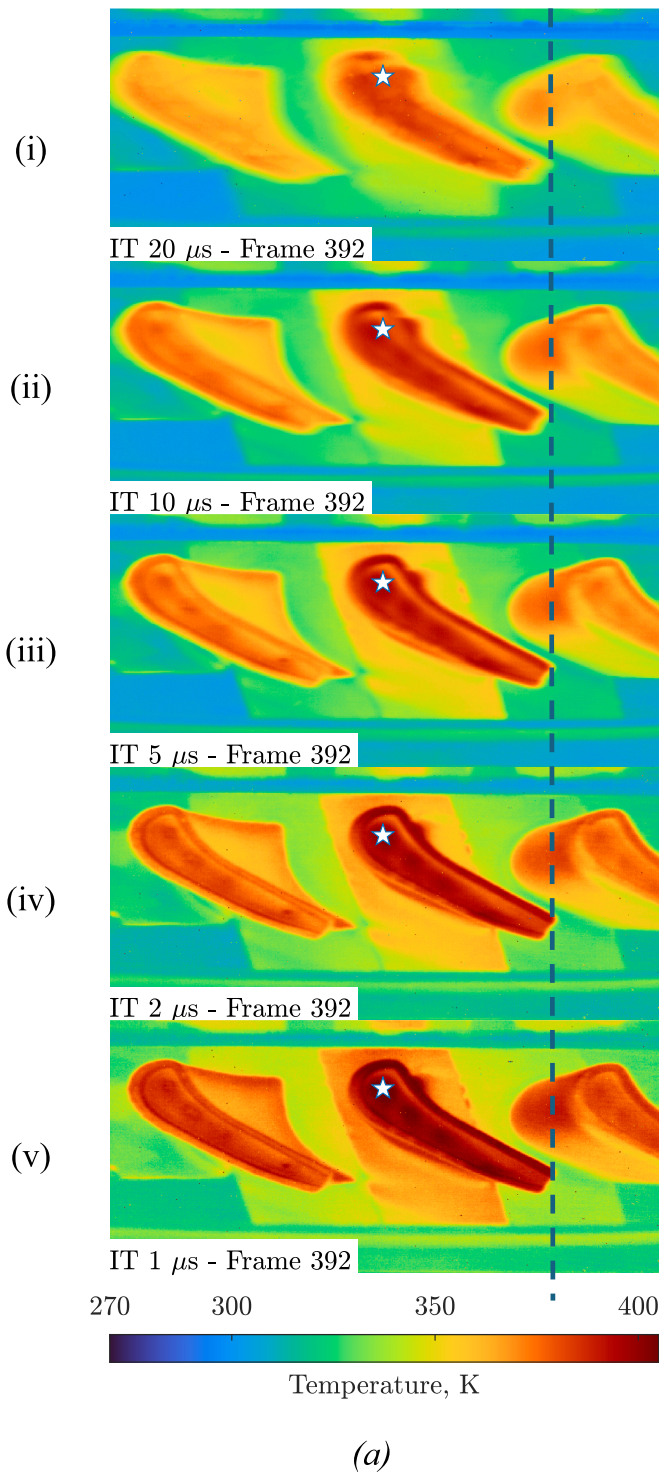


Fig. 12. Effect of camera integration time on image quality and signal level: (a) Infrared images of T_{cam1} at frame 392 from different runs, recorded with various integration times; (b) temporal history of T_{cam1} for pixel marked by star in (a); (c-d) detector saturation levels for the star-marked pixel as a function of integration time and nondimensional blur d^* shown across different stages of the test.

reference to the blade tip edge pressure side corner at the shortest integration time across all images. As the run-to-run variability of turbine inlet temperature in the OTRF is $\pm 2\%$, the variation observed in the measured T_{cam} is a result of the measurement sensitivity to camera integration time.

Notably, in image (i) with the longest integration time (20 μs), the blade edges display considerable blur, progressively sharpening as the integration time decreases. The translational shift in blade position from

right to left with increasing integration time provides a measure for the level of blur at 2.7 mm and 4.5 mm for integration times of 10 μs and 20 μs , respectively, comparing well with the pre-test estimates in Table 3. Although image (v) with the shortest integration time (1 μs) is clearly the sharpest, it also exhibits the lowest signal-to-noise ratio. This is evident in Fig. 12(b), which depicts the temporal history of T_{cam} for the surveyed pixel located at a local hot spot in the blade gutter near the leading edge, indicated by a star symbol. The reduced signal quality

results from lower detector saturation, particularly evident during the initial spin up phase of the test, when the lowest temperature values are recorded. Conversely, the longer integration times of 20 μs and 10 μs yield blade displacement large enough for local temperature gradients to cause measurement errors within the main test period at the surveyed pixel, in the order of 10 K in T_{cam} . Qualitatively, image (iii) with an integration time of 5 μs is ideal for balancing noise and motion blur at this speed.

The temporal plots shown in Fig. 12(b) also reveal a discrepancy with the temperature values in the initial spin up phase (prior to frame 200). The lowest integration time dataset records a blackbody equivalent temperature of approximately 319 K compared to approximately 302 K recorded in the dataset for the longest integration time (pre-test wall temperatures recorded by thermocouples agreed to within ± 2 K). The difference is attributable to the larger measurement error with shorter integration times, especially evident at lower temperatures. This behaviour agrees with the characterisation of the temporal error from the detector, which decreases as integration time and target temperature increases.

Fig. 12(c) shows the detector saturation at the surveyed pixel as a function of integration time for the three phases of the test: spin up, coolant injection, and run. The grey band highlights the saturation range yielding a detector temporal error lower than 2 K (detector saturation greater than 5%), while the red dashed line represents the manufacturer's recommended minimum level. Fig. 12(d) presents the same data as Fig. 12(c), expressed as a function of the nondimensional blur parameter d^* , calculated based on the squealer tip width $d = 1.3$ mm. The light blue region highlights the acceptable minimum blur ($0 < d^* < 1.2$). Points located within the overlapping area of the grey and light blue regions satisfy both criteria for acceptable blur and detector saturation.

Comparing different phases of the test, an integration time of 5 μs (image iii) offers an optimal balance between image blur and detector saturation during the steady portion of the run, with the spin-up and coolant injection phases being just on the border of this region with a 4.4% (spin-up stage) and 4.01% (coolant injection stage) detector saturation. To determine surface heat flux, reliable data from the early part of the time history are required, where target temperatures are lower. Therefore, the requirements for the balance between measurement errors due to image blur and detector saturation must be considered and optimised based on the specific objective of the experiment. For instance, evaluation of metal effectiveness (i.e. non-dimensional surface temperature) only requires data within the main test period, permitting more flexibility in selecting a shorter integration time.

The following heat transfer analysis focusses on evaluating the impact of camera integration time on key heat transfer quantities, including heat flux, adiabatic wall temperature and Nusselt number. The analysis is based on data acquired at the rotor tip in the OTRF using camera integration time of 1 μs , 5 μs , and 10 μs .

6. Impact of Camera Integration Time on Adiabatic Wall Temperature and Nusselt Number

The camera synchronisation system was able to capture one image per revolution of any selected blade with an error of ± 5 pixels (± 0.55 mm on the blade tip). Additionally, during the test period the onset of the mainstream flow induced vibrations in the camera mounting resulting in translational movement by approximately ± 9 pixels ($\approx \pm 1$ mm on the blade tip). Processing to heat transfer requires accurate time history. In areas of high gradients, e.g. blade tip edges, even this instability can cause errors. To minimise the impact of the displacement on measurement accuracy, the motion tracking algorithm within the Blender software was employed. The detected displacement was corrected in MATLAB, where each frame was spatially re-aligned and stabilised. Subsequently, stabilised videos were re-imported into Blender for post-correction verification, typically demonstrating displacement

reduction in both directions to a maximum of ± 1 px.

The processing of surface temperature measurements to heat flux involves solving the heat transfer conduction equation using the impulse response method by Oldfield [29]. The method entails determining the impulse response function $g(t)$ of the substrate from a step function in $\dot{q}(t)$ and corresponding analytical solution for transient surface temperature $T(t)$ for a semi-infinite substrate, performed using FFT based filtering in MATLAB. Once known, convolution of this function with the measured temperature history provides the experimental heat flux $q(t) = g(t) * T(t)$.

Having evaluated the transient surface heat flux $\dot{q}(t)$ during the pseudo-steady test period, the adiabatic wall temperature, T_{aw} , and the heat transfer coefficient, h , can be found by linear regression of $\dot{q}(t)$ and $T_t(t)$, based on the thermal convection equation (Newton's law of cooling):

$$\dot{q}(t) = h(T_t(t) - T_{aw}) \quad (3)$$

Corrected infrared surface temperature maps for the blade tip for a single frame acquired during the stable main test period for a typical run with uniform inlet conditions and camera integration times of 10 μs , 5 μs , and 1 μs are shown in Fig. 13. The IR camera is not calibrated in situ, and different integration times lead to different results in target temperature measurements. Specifically, longer integration times introduce error due to blurring effects with averaging of high-low temperature zones, while shorter integration times introduce error due to the detector undersaturation (low signal to noise ratio). The latter issue is particularly significant at lower temperatures (detector saturation less than $\sim 15\%$ full scale), where the detector calibration, that assumes fitting to 4th order polynomial as energy reaching sensor is proportional to T^4 , is significantly less accurate due to systematic errors in the camera detector electronics (see Fig. 11). In this instance, an integration time of 5 μs provides the best balance between blur and measurement accuracy. This is further inferred from the results of heat transfer and from the uncertainty analysis in surface temperature presented in the following section. It is interesting to note that the thermal maps in Fig. 13 capture the typical overtow flow patterns, which are most distinguishable in Fig. 13(b). The temperature on the squealer rim is hottest near the leading edge (a) and along the pressure side (b), likely resulting from tip leakage flow moving from pressure to suction side (c) over the tip of the blade. Entering the squealer cavity (d), the leakage flow separates resulting in a region of lower surface temperature before reattachment causing higher surface temperatures again.

The regression analysis to determine adiabatic wall temperature and heat transfer coefficient for pixel r – as labelled in Fig. 13 – is summarised in Fig. 14 for a range of integration times. Plots include: target temperature as a function of time in Fig. 14(a), transient heat flux calculated using the impulse response method in Fig. 14(b), and linear regression of heat flux and target temperature in Fig. 14(c). The vertical black dashed lines in Fig. 14(a) and (b) mark the period of pseudo-steady aerodynamic conditions during which regression data is taken. The frequency response of the current technique is limited by the available framerate of the infrared camera, restricting its application to the evaluation of time-averaged heat flux. However, it offers the advantage of providing full two-dimensional measurements. In contrast, thin-film heat flux gauges enable high-frequency response, but only offer point-based measurements. To date, when applied to rotor surfaces, thin-film gauges have failed to achieve enough temperature rise during the stable portion of the run, to enable accurate regression to adiabatic wall temperature. The superiority of IR thermography in this context has been demonstrated by Sisti et al. [34], who compared the current technique to in-view thin-film gauges measurements, as well as to numerical simulations.

The differences in $T_{cam}(t)$ with integration time have been discussed. Of interest is the subsequent effect these differences have on the calculated adiabatic wall temperature and heat transfer coefficient by the

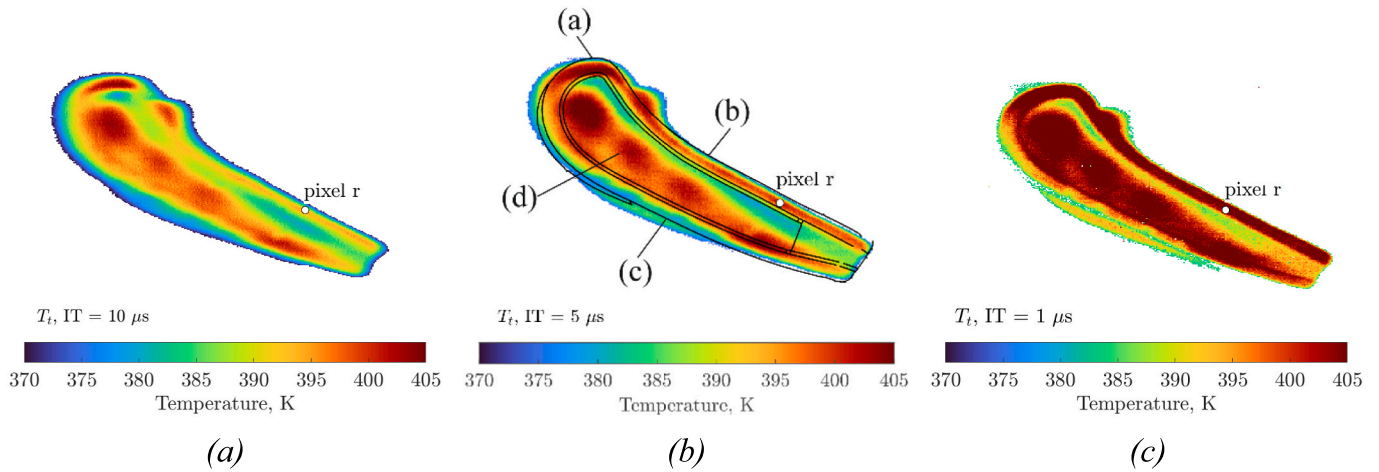


Fig. 13. Temperature T_t of blade tip at frame 392. Camera integration time of (a) $10 \mu s$, (b) $5 \mu s$, and (c) $1 \mu s$. One pixel highlighted for point analysis.

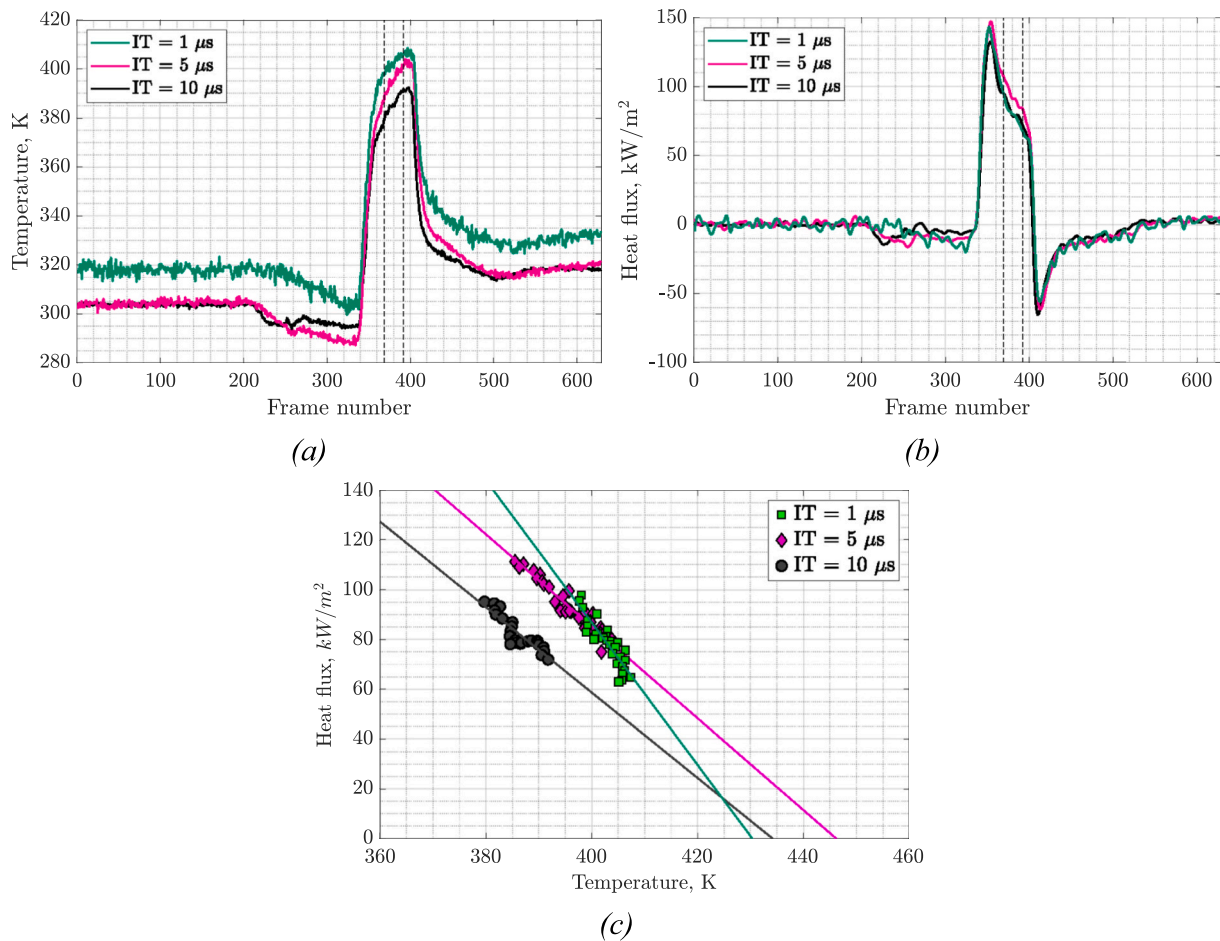


Fig. 14. Heat transfer analysis for one pixel on blade tip and for three camera integration times: (a) surface temperature $T_t(t)$; (b) heat flux $\dot{q}(t)$; (c) $\dot{q}(T_t(t))$ to obtain h and T_{aw} by extrapolation, with regression data only.

regression of $T_t(t)$ and $\dot{q}(t)$. For all three camera integration times, the surface heat flux – plotted in Fig. 14(b) – is initially zero as the temperature histories are steady until the onset of the main hot test gas, which causes a sharp rise in heat flux followed by a steady reduction as the surface temperature rise tends towards the adiabatic condition. The differences in measured $T_t(t)$ with varying integration time cause small but influential differences in $\dot{q}(t)$ during the window used for data

regression. With the longest integration time of $10 \mu s$, the lower surface temperature measured within the regression window due to extensive blur causes a reduced heat flux compared to an integration time of $5 \mu s$. With the shortest integration time of $1 \mu s$, error in the initial surface temperature measurement due to detector undersaturation also causes a reduced heat flux compared to an integration time of $5 \mu s$. With an integration time of $5 \mu s$, blur is minimised without causing error due to

detector undersaturation. This result agrees with the assessment from the previous section, deeming 5 μs as the best compromise for this particular experiment.

Fig. 14(c) show the sensitivity of errors in $T_t(t)$ and calculated $\dot{q}(t)$ on the regression to determine adiabatic wall temperature ($\dot{q}=0$) and heat transfer coefficient – given by the gradient of the linear regression. Interestingly, although the adiabatic wall temperature is underpredicted by ~ 12 K for an integration time of 10 μs compared to 5 μs due to the image blur, the determined heat transfer coefficients agree to within $\pm 10\%$. The sensitivity to detector undersaturation is much stronger, with an overprediction of adiabatic wall temperature of ~ 16 K and heat transfer coefficient by 56%. Scaled to engine conditions, such errors would likely result in either significant over-cooling of components to the detriment of engine efficiency, or significant under-cooling drastically affecting component life.

The calculation for adiabatic wall temperature was extended to the entirety of the FOV, obtaining the two-dimensional maps depicted in Fig. 15. The hottest regions are the squealer rim on the pressure side and towards the trailing edge, as well as the region in the squealer cavity towards the leading edge. The maps obtained processing the 10 μs and 1 μs camera integration time thermal data show the highest values of adiabatic wall temperature, with maximum values of approximately 540 K which is unphysical given the turbine inlet temperature conditions (see Table 2). This is a consequence of the observed errors in surface temperature measurements. In the dataset acquired with 10 μs integration time, the observed errors in surface temperature measurements are primarily caused by spatial averaging across regions with steep temperature gradients during the run. This effect arises from significant image blur: with a nondimensional blur parameter $d^* = 2.03$, the squealer rim travels more than twice its width during the exposure time. As a result, the detector collects radiance contributions from both the hotter tip region and the adjacent colder platform region, leading to inaccurate temperature reading.

The results achieved with the 1 μs camera integration time dataset also present a higher level of noise as expected with significant detector undersaturation. Again, with a 5 μs camera integration time, results are within physical bounds with a maximum adiabatic wall temperature value of 479 K, and display a balance between sources of error.

Finally, the adiabatic wall temperature was used to reduce the heat flux data to a scalable non-dimensional Nusselt number, based upon the rotor true chord, defined as:

$$Nu = \frac{hc_{true}}{k_{air}} = \frac{\dot{q}(t) c_{true}}{k_{air}(T_{aw} - T_t(t))} \quad (4)$$

Maps of Nusselt number for the squealer tip, averaged over the stable portion of the run are shown in Fig. 16. As for the maps of adiabatic wall temperature, the map calculated using data captured with a camera

integration time of 1 μs is clearly affected by noise. Furthermore, both maps obtained with data captured with 10 μs and 1 μs camera integration times present regions of significantly higher and lower Nusselt number values compared to the 5 μs case, which could impact engine efficiency and/or life when applied to engine design. This demonstrates the importance of selecting an appropriate camera integration time to minimise measurement error, which in the present experiments was achieved at 5 μs .

7. Uncertainty in Surface Temperature

The post-test uncertainty analysis in surface temperature is based on the uncertainty values for emissivity U_e , transmissivity U_t , and blackbody equivalent temperature $U_{T_{com}}$, evaluated for the calibration methodology developed and characterised by Sisti et al. [1]. Alongside these values, the maximum error in blackbody equivalent temperature $U_{T_{com,IT}}$, characterised in Fig. 10, and a typical error in the optical path temperature reading from thermocouple $U_{T_{opt}}$ of ± 2 K were used. The uncertainty analysis was developed according to the equations detailed in the Appendix. Uncertainty values were calculated for each pixel on the rotor tip for data obtained with integration times of 10, 5 and 1 μs , thus providing two-dimensional error maps as a function of time. These maps are shown in Fig. 17(a)-(c) for a frame selected during the stable portion of the run, same as selected for previous figures. Fig. 17(d)-(f) shows the temporal history of both T_t and the error in surface temperature corresponding to the pixel highlighted in the corresponding error map. From top to bottom, integration time decreases from 10 μs to 1 μs . Note that the error maps have different colour bar limits, necessary as the values to display are too different in this case. Increasing uncertainty with decreasing integration time is evident, with maximum uncertainties of 5 K (1.7%), 6.72 K (2.3%), and 12 K (3.9%) for integration times of 10 μs , 5 μs and 1 μs respectively, experienced during spin up/coolant injection (frames 0–330) at near ambient conditions. During the stable period of the test uncertainties reduce to 3.35 K (0.88%), 3.8 K (0.99%) and 6 K (1.5%). However, these values do not include error due to image blur that corrupts the data at the higher integration time in the run phase where a large spatial temperature gradient is observed between the blade tip and platform regions.

This analysis confirms that an integration time of 5 μs offers the most suitable balance for the measurements presented, aligning with the detector saturation trends discussed in Section 5. These results are consistent with the calibration findings reported by Sisti et al. [1], demonstrating that both longest and shortest integration times lead to inherent errors, due to blur in the former and to high temporal error in the latter. For test conditions requiring good accuracy across the full experimental time history, specifically at target speeds on the order of 260 m/s and features size on the order of 1.3 mm, an integration time of 5 μs is optimal. For experiments focusing on quantities such as coolant

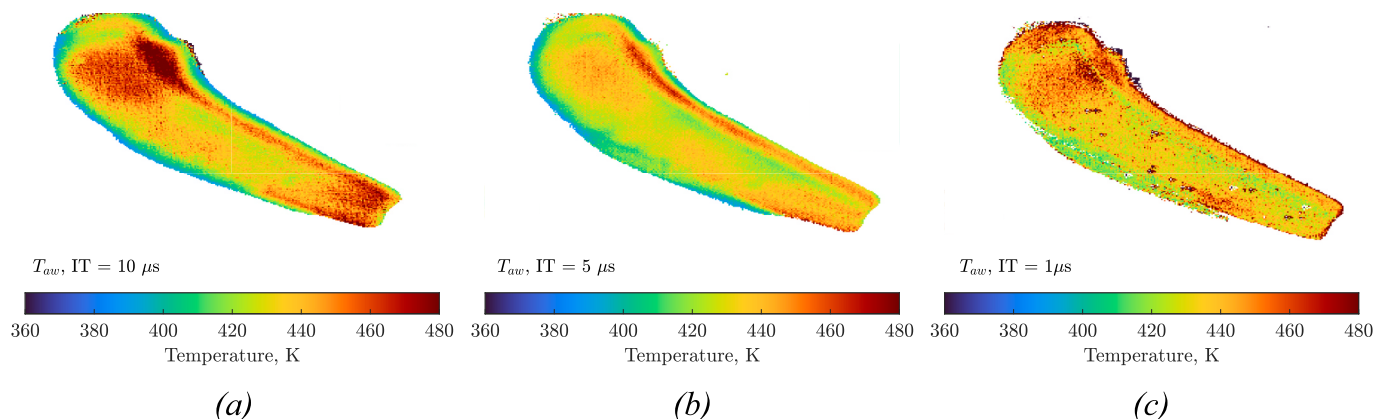


Fig. 15. 2D maps of adiabatic wall temperature on the rotor blade tip, obtained with data captured with a camera integration time of (a) 10 μs , (b) 5 μs , and (c) 1 μs .

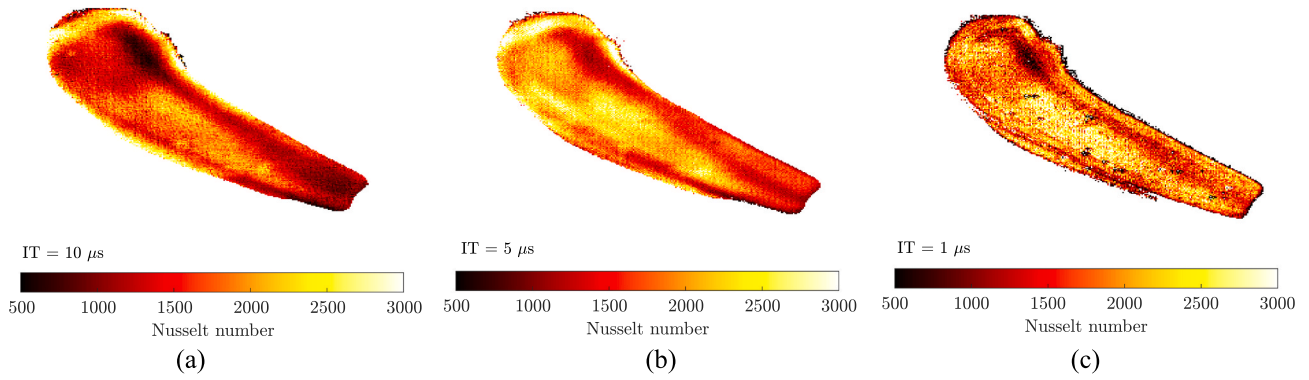


Fig. 16. 2D maps of Nusselt number on the rotor blade tip, obtained with data captured with a camera integration time of (a) 10 μs , (b) 5 μs , and (c) 1 μs .

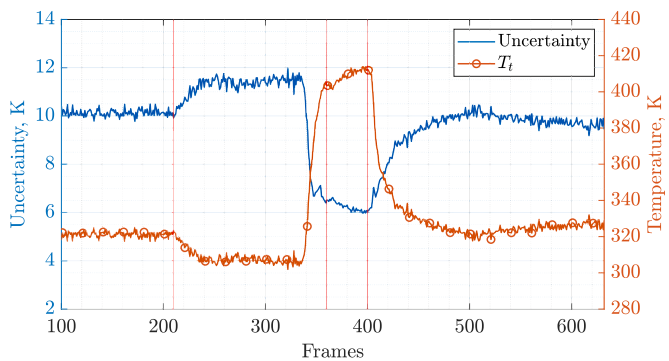
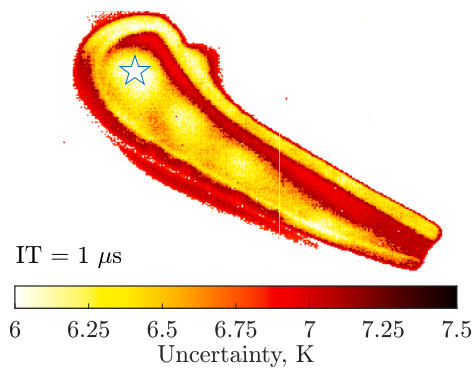
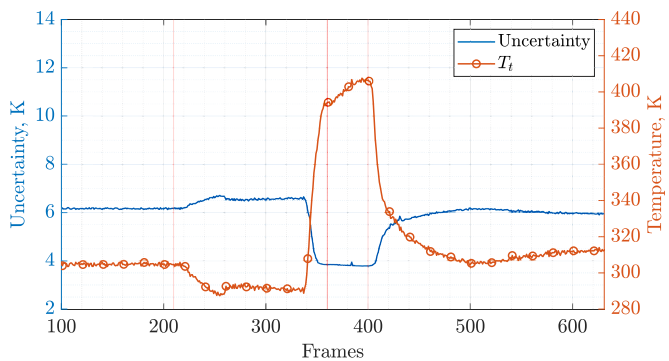
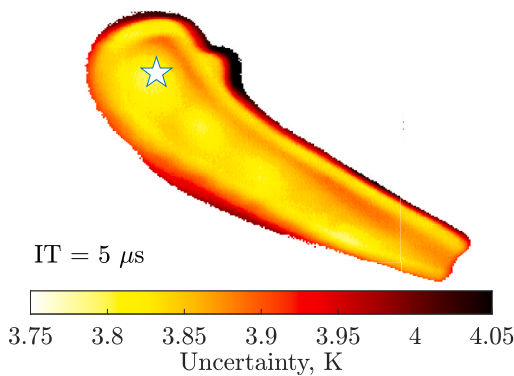
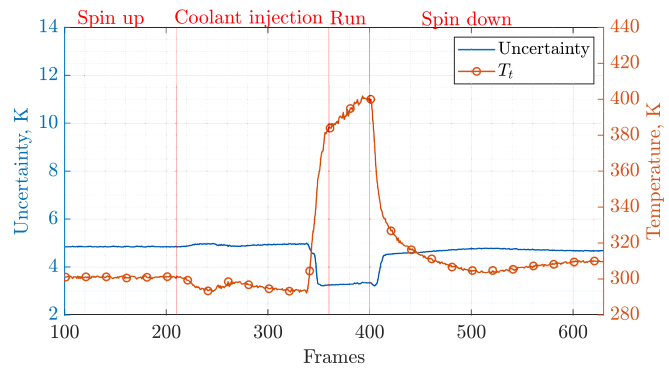
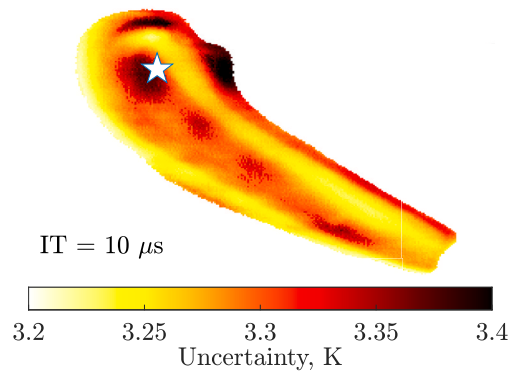


Fig. 17. Total error in surface temperature measurements Left: maps of error for frame 392. Right: temporal history of error and surface temperature for pixel marked by star symbol on the correspondent image. Top to bottom: integration times 10, 5, and 1 μs .

and metal effectiveness, which do not require knowledge of the full-time history, a lower integration time may also be appropriate.

These measurements represent an important leap forward in the field of turbomachinery research. Never was this type of measurement possible within experimental test facilities such as the OTRF. The significance of this achievement becomes evident when considering the abundance of insights now accessible with full surface thermal maps, and the simplification of the system compared to the historical approach using point-based thin-film gauges with associated wiring, in-shaft signal conditioning and telemetry systems.

8. Conclusions

In this paper, the first experimental IR thermography data of rotor tip in the Oxford Turbine Research Facility has been presented. The facility was operated at nominal rotational speed of 8,500 rpm, thus blade tip nominal velocity of 263.5 m/s, and gas temperature at NGV inlet ranging from 295 K to 475 K during testing.

Raw digital counts two-dimensional maps of rotor blade tips were acquired for camera integration times ranging from 20 μ s, leading to blur of 5.27 mm, to 1 μ s, presenting virtually no blur (0.26 mm). This data was processed to corrected target temperature following the methodology presented by Sisti et al. [1]. An overall maximum correction of approximately 1.13% was identified between blackbody equivalent and target temperature.

To evaluate the detector performance as a function of camera integration times and blackbody temperature, the detector temporal error was investigated. This error arises from the inability of the detector to distinguish between noise and signal level when fewer photons are collected by the sensing element, a condition verified at low camera integration time and/or low target temperatures. For a typical pixel this error was found to be as high as ± 10 K at temperatures of 293 K and camera integration time of 1 μ s, decreasing to approximately ± 2 K at temperatures of 293 K and camera integration time of 20 μ s. It was demonstrated that a detector saturation greater than 5% is needed to achieve a temporal error lower than 2 K.

Equivalent blackbody temperature maps and time histories of blade tips from different runs under identical operating conditions acquired the OTRF were compared to evaluate the impact of the camera integration time on image quality and temperature measurement accuracy. Results were shown for camera integration times of: 20, 10, 5, 2, and 1 μ s. Longer integration times (20 μ s and 10 μ s) result in noticeable blade displacement, which introduces errors of approximately 10 K during the main test period due to spatial averaging over steep local temperature gradients. Conversely, shorter integration times (1 μ s) show differences of up to 17 K in equivalent blackbody temperature readings at the beginning of the test period when compared to longer integration times (20 μ s). Analysing the detector saturation achieved in each test, it was concluded that the integration time of 5 μ s satisfied the requirement of 5% detector saturation, offering an optimal balance between image blur and measurement accuracy.

Surface temperature maps were then process to heat flux, adiabatic wall temperature, and Nusselt number. Results were shown at camera

Appendix. – Uncertainty Calculations

Governing equation:

$$T_t = \left(\frac{1 - \varepsilon_2}{\tau(\varepsilon_1 - \varepsilon_2)} T_{cam1}^4 - \frac{1 - \varepsilon_1}{\tau(\varepsilon_1 - \varepsilon_2)} T_{cam2}^4 - \frac{1 - \tau}{\tau} T_{opt}^4 \right)^{0.25}$$

integration times of 10 μ s, 5 μ s, and 1 μ s for the entire field of view as well as for one pixel on the blade squealer rim. For all three integration times, the hottest regions were the squealer rim on the pressure side, as well as inside the squealer cavity towards the leading edge. Adiabatic wall temperatures for a pixel on the rim towards the trailing edge was approximately 434 K, 446 K, and 430 K, at camera integration times of 10 μ s, 5 μ s, and 1 μ s, respectively. These results prove that longest and shortest integration time present errors due to blur in the first instance and low temperature/high temporal error in the second instance. In both cases, this reflects in the values achieved of adiabatic wall temperature and Nusselt number. A balance of these two conditions is achieved with the 5 μ s camera integration time.

Finally, this behaviour was further characterised by a post-test uncertainty analysis carried out on the surface temperature measurements. For a pixel in the squealer tip cavity, the error analysis showed that during the cold phase of the run errors go from 5 K (1.7%) to 12 K (4%) with decreasing integration time. Generally, lower errors are found in the hot phase of the test, going from 3.35 K (0.88%) at 10 μ s to 6 K (1.5%) at 1 μ s. These findings highlight the capability of IR thermography to resolve temperature of fast moving targets underlying the importance of balancing camera integration time to minimise errors from motion blur and temporal response in IR thermography for high-speed rotating blades. Building on the current findings, future work will aim to quantify the contribution of image blur to the overall measurement uncertainty and explore deblurring methodologies which may be required to image very small features. Additionally, the possibility of developing calibration methodologies to correct detector temporal errors at very short integration times will be investigated. One possible strategy for post-correcting the infrared temperature measurements would involve first conducting a repeatability study on the detector temporal error, which could then support the development of pixel-wise calibration curves for the temporal error.

CRedit authorship contribution statement

Manuela Sisti: Writing – review & editing, Writing – original draft, Methodology, Investigation, Formal analysis, Data curation, Conceptualization. **Chiara Falsetti:** Writing – review & editing, Writing – original draft, Supervision, Conceptualization. **Paul F. Beard:** Writing – review & editing, Writing – original draft, Supervision, Project administration, Methodology, Conceptualization.

Declaration of competing interest

The authors declare that they have no known competing financial interests or personal relationships that could have appeared to influence the work reported in this paper.

Acknowledgements

The authors would like to acknowledge Rolls-Royce plc and EPSRC for funding this research.

Equations for uncertainty in surface temperature.

Expected values with errors	Target temperature with error
$\varepsilon_1^* = \varepsilon_1 + U_\varepsilon$	$T_{t,\varepsilon_1^*} = \left(\frac{1 - \varepsilon_2}{\tau(\varepsilon_1^* - \varepsilon_2)} T_{cam1}^4 - \frac{1 - \varepsilon_1^*}{\tau(\varepsilon_1^* - \varepsilon_2)} T_{cam2}^4 - \frac{1 - \tau}{\tau} T_{opt}^4 \right)^{0.25}$
$\varepsilon_2^* = \varepsilon_2 + U_\varepsilon$	$T_{t,\varepsilon_2^*} = \left(\frac{1 - \varepsilon_2^*}{\tau(\varepsilon_1 - \varepsilon_2^*)} T_{cam1}^4 - \frac{1 - \varepsilon_1}{\tau(\varepsilon_1 - \varepsilon_2^*)} T_{cam2}^4 - \frac{1 - \tau}{\tau} T_{opt}^4 \right)^{0.25}$
$\tau^* = \tau + U_\tau$	$T_{t,\tau^*} = \left(\frac{1 - \varepsilon_2}{\tau^*(\varepsilon_1 - \varepsilon_2)} T_{cam1}^4 - \frac{1 - \varepsilon_1}{\tau^*(\varepsilon_1 - \varepsilon_2)} T_{cam2}^4 - \frac{1 - \tau^*}{\tau^*} T_{opt}^4 \right)^{0.25}$
$T_{opt}^* = T_{opt} + U_{T_{opt}}$	$T_{t,T_{opt}^*} = \left(\frac{1 - \varepsilon_2}{\tau(\varepsilon_1 - \varepsilon_2)} T_{cam1}^4 - \frac{1 - \varepsilon_1}{\tau(\varepsilon_1 - \varepsilon_2)} T_{cam2}^4 - \frac{1 - \tau}{\tau} T_{opt}^{*4} \right)^{0.25}$
$T_{cam1}^* = T_{cam1} + U_{T_{cam1}} + U_{T_{cam1},IT}$	$T_{t,T_{cam1}^*} = \left(\frac{1 - \varepsilon_2}{\tau(\varepsilon_1 - \varepsilon_2)} T_{cam1}^{*4} - \frac{1 - \varepsilon_1}{\tau(\varepsilon_1 - \varepsilon_2)} T_{cam2}^4 - \frac{1 - \tau}{\tau} T_{opt}^4 \right)^{0.25}$
$T_{cam2}^* = T_{cam2} + U_{T_{cam2}} + U_{T_{cam2},IT}$	$T_{t,T_{cam2}^*} = \left(\frac{1 - \varepsilon_2}{\tau(\varepsilon_1 - \varepsilon_2)} T_{cam1}^4 - \frac{1 - \varepsilon_1}{\tau(\varepsilon_1 - \varepsilon_2)} T_{cam2}^{*4} - \frac{1 - \tau}{\tau} T_{opt}^4 \right)^{0.25}$

Where: $U_\varepsilon = \pm 0.013$; $U_\tau = \pm 0.013$; $U_{T_{opt}} = \pm 2K$; $U_{T_{cam1}} = \pm 2K$; $U_{T_{cam1},IT}$ is taken for data shown in Fig. 10. Finally, the total uncertainty in target temperature is as follow

$$U_{T_t} = \sqrt{\left(T_t - T_{t,\varepsilon_1^*}\right)^2 + \left(T_t - T_{t,\varepsilon_2^*}\right)^2 + \left(T_t - T_{t,\tau^*}\right)^2 + \left(T_t - T_{t,T_{opt}^*}\right)^2 + \left(T_t - T_{t,T_{cam1}^*}\right)^2 + \left(T_t - T_{t,T_{cam2}^*}\right)^2}$$

Data availability

The data used is commercially sensitive.

References

[1] M. Sisti, C. Falsetti, P.F. Beard, Infrared temperature measurements on fast moving targets: A novel calibration approach, *Measurement* 225 (2024) 113870.

[2] National Academies of Sciences, Engineering and Medicine, Commercial Aircraft Propulsion and Energy Systems Research: Reducing Global Carbon Emissions, Washington, DC: The National Academies Press, (2016). <https://doi.org/10.17226/23490>.

[3] P.T. Ireland, T.V. Jones, Liquid crystal measurements of heat transfer and surface shear stress, *Meas. Sci. Technol.* 11 (2000) 969–986.

[4] M. Kunze, K. Vogeler, G. Brown, C. Prakash, K. Landis, Aerodynamic and Endwall film-cooling investigations of a gas turbine nozzle guide vane applying temperature-sensitive paint, *J. Turbomach.* 133 (3) (2011) 031027.

[5] C.R. Smith, D.R. Sabatino, T.J. Praisner, Temperature sensing with thermochromic liquid crystals, *Exp. Fluids* 30 (2001) 190–201.

[6] Z. Gao, D.P. Narzary, J.C. Han, Film cooling on a gas turbine blade pressure side or suction side with compound angle shaped holes, *J. Turbomach. ASME* 131 (2009).

[7] N. Gurram, P.T. Ireland, T.H. Wong, K.P. Self, Study of film cooling in the trailing edge region of a turbine rotor blade in high speed flow using pressure sensitive paint. *Proceedings of the ASME Turbo Expo*, 2016.

[8] J.C. Han, A. Rallabandi, Turbine blade film cooling using PSP technique, *Front. Heat Mass Transfer* 11 (1) (2010) 1–21.

[9] L. Yang, L. Zhi-min, The research of temperature indicating paints and its application in aero-engine temperature measurement, *Procedia Eng.* 88 (2015) 1152–1157.

[10] C. Falsetti, M. Sisti, P.F. Beard, Infrared thermography and calibration techniques for gas turbine applications: A review, *Infrared Phys. Technol.* 113 (2021) 103574.

[11] G. Cardone, T. Astarita, G.M. Carlomagno, Heat transfer measurements on a rotating disk, *Int. J. Rotating Mach.* 3 (1997) 1–9.

[12] T. Astarita, G. Cardone, G. Carlomagno, Spiral vortices detection on a rotating disk, in: 23rd International Congress of Aeronautical Sciences, (2002) Toronto, ON, Canada.

[13] G. Carlomagno, G. Cardone, Infrared thermography for convective heat transfer measurements, *Exp. Fluids* 49 (2010) 1187–1218.

[14] R.J. Boyle, C.M. Spuckler, B.L. Lucci, W.P. Camperchioli, Infrared low-temperature turbine turbine vane rough surface heat transfer measurements, *J. Turbomach.* 123 (1) (2001) 168–177.

[15] S.V. Ekkad, S. Ou, R.B. Rivir, A transient infrared thermography method for simultaneous film cooling effectiveness and heat transfer coefficient measurements from a single test, *J. Turbomach.* 126 (2004) 597–603.

[16] M. Mori, L. Novak, M. Sekavcnik, Measurements on rotating blades using IR thermography, *Exp. Therm Fluid Sci.* 32 (2007) 387–396.

[17] M. Mori, L. Novak, M. Sekavcnik, I. Kuštrin, Application of IR thermography as a measuring method to study heat transfer on rotating surface, *Forsch. Ingenieurwes.* 72 (2008) 1–10.

[18] S. Lazzi Gazzini, R. Schader, A.L. Kalfas, R.S. Abhari, Infrared thermography with non-uniform heat flux boundary conditions on the rotor endwall of an axial turbine, *Meas. Sci. Technol.* 28 (2017) 025901.

[19] B.F. Knisely, R.A. Berdanier, K.A. Thole, C.W. Haldeman, J.R. Markham, J. E. Cosgrove, A.E. Carlson, J.J. Scire, Acquisition and processing considerations for infrared images of rotating turbine blades, *ASME J. Turbomach.* 143 (2021) 041013.

[20] B.F. Knisely, R.A. Berdanier, K.A. Thole, C.W. Haldeman, Effects of part-to-part flow variation on overall effectiveness and life of rotating turbine blades. *Proceedings of ASME Turbo Expo 2022*, 2022.

[21] L. Christensen, R. Celestina, S. Sperling, R. Mathison, H. Aksoy, J. Liu, Infrared temperature measurements of the blade tip for a turbine operating at corrected engine conditions, *J. Turbomach.* 143 (2021) 101005, <https://doi.org/10.1115/1.4050675>.

[22] L. Christensen, R. Celestina, S. Sperling, R. Mathison, H. Aksoy, J. Liu, J. Nickol, Comparison of Computational Predictions for a Cooled High-Pressure Turbine to Data From a Short Duration Experiment, in: *Turbo Expo: Power for Land, Sea, and Air*, Boston, (2023) Massachusetts, USA. <https://doi.org/10.1115/GT2023-103994>.

[23] R. J. Anthony, C. Haldeman, Hot Section Thermal Imaging Technology Development: Lessons and Implications for Engine Focused Transient Measurement Techniques, in: *ASME Turbo Expo*, Boston, (2023). <https://doi.org/10.1115/GT2023-103186>.

[24] R. J. Anthony, N. Vanasse, S. McClaren, High Speed Rotating HPT Blade Thermal Imaging of a Full Scale Cooled 1+1/2 Stage Turbine in a Short Duration Transient Test Facility, in: *ASME Turbo Expo*, (2024) London.

[25] M.G. Adams, T. Povey, B.F. Hall, D.N. Cardwell, K.S. Chana, P.F. Beard, Commissioning of a combined hot-streak and swirl profile generator in a transonic turbine test facility, *ASME J. Eng. Gas Turb. Power* 142 (2020), 031008-1-16.

[26] C. Falsetti, P.F. Beard, D.N. Cardwell, K.S. Chana, A Review of High-Speed Rotating HP Turbine Heat Transfer and Cooling Studies Over the Last Decade in the Oxford Turbine Research Facility. *Proceedings of the ASME Turbo Expo 2022: Turbomachinery Technical Conference and Exposition*, 2022.

[27] D.C. Harris, Materials for infrared windows and domes, *Propert. Perform.* (1999).

[28] S. Shahpar, S. Caloni, Aerodynamic optimization of high-pressure turbines for lean-burn combustion system, *J. Eng. Gas Turbines Power* 135 (2013) 055001.

[29] M.L.G. Oldfield, Impulse response processing of transient heat transfer gauge signals, *J. Turbomach.* 130 (2008).

[30] D.L. Schultz, T.V. Jones, Heat-transfer measurements in short duration hypersonic facilities, *AGARD-AG-165 AG* (1973).

[31] D. Singh, P. Beard, D. Cardwell, V. Staelens, P. Bahulekar, M. Stokes, S. Bather, K. Chana, An Aerodynamic Investigation of a High-Pressure Turbine using Rotor Casing Static Pressure Measurements at Engine Representative Conditions with Different Tip Designs, Tip Gaps and Inlet Temperature Profiles, in: *Proceedings of ASME Turbo Expo 2024*, June 24–28, (2024) London, UK.

[32] S. Gao, L. Wang, C. Feng, K. Daniel, Analysis and improvement of gas turbine blade temperature measurement error, *Meas. Sci. Technol.* 26 (10) (2015) 105–203.

[33] Crystran, Zinc Selenide material properties, (2023).

[34] M. Sisti, R. Adoua, C. Falsetti, H. Li, P. Beard, Impact of Turbine Inlet Temperature Distortion on Rotor Blade Heat Transfer at Engine Representative Conditions Using Infrared Thermography, in: *Proceedings of the 16th European Turbomachinery Conference (ETC16) Turbomachinery, Fluid Dynamics and Thermodynamics*, (2025) Hannover.